

# XROTOR

X-shaped Radical Offshore Wind Turbine for Overall Cost of Energy Reduction

D3.2

## Control simulation model for X-ROTOR concept

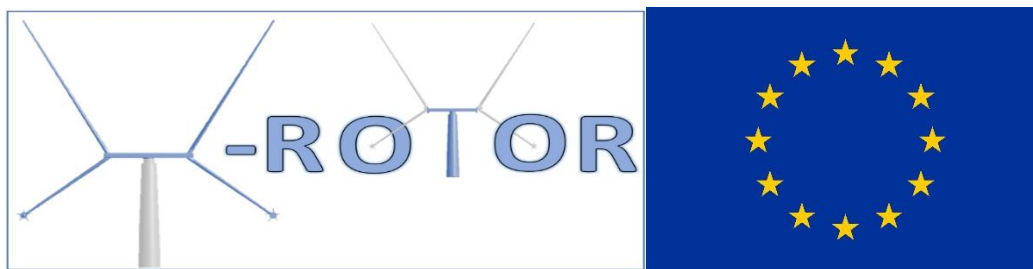
 <https://xrotor-project.eu>

 @XROTORProject

**March 2022**



This project has received funding from the European Union's Horizon 2020 research and innovation programme under grant agreement No 101007135



## Project Coordinator Approval Form

Project acronym: **XROTOR**  
 Grant agreement number: 101007135  
 Start date: 01<sup>st</sup> January 2021  
 Duration: 3 years

### Document Information

Date	Description	Prepared by	Reviewed by	Approved by
31/03/2022	Final version	University of Strathclyde	W. Leithead (Project Coordinator)	J. Carroll  (Project Coordinator)

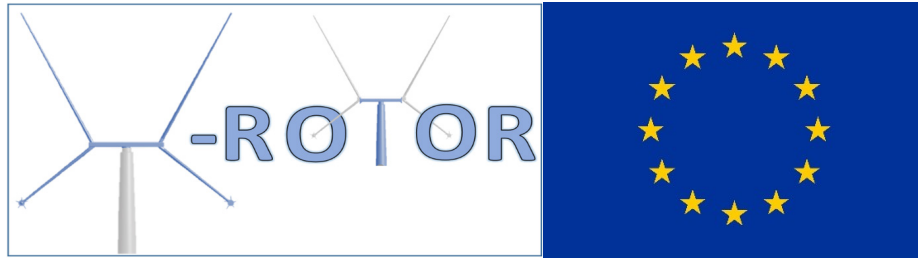
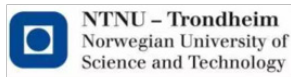


The X-ROTOR Project has received funding from the European Union's Horizon 2020 research and innovation programme under grant agreement no. 101007135. For more information on the project, its partners, and contributors please see <https://XROTOR-project.eu>.

### Disclaimer

The information contained in this document represents the views of X-ROTOR consortium as of the date they are published. The X-ROTOR consortium does not guarantee that any information contained herein is error-free, or up to date, nor makes warranties, express, implied, or statutory, by publishing this document. The information in this document is provided as is and no guarantee or warranty is given that the information is fit for any particular purpose. The user thereof uses the information at its sole risk and liability.

The sole responsibility for the content of this publication lies with the authors. It does not necessarily reflect the opinion of the European Union. Neither the European Commission nor its executive agencies are responsible for any use that may be made of the information contained therein.



# X-ROTOR: X-shaped Radical Offshore wind Turbine for Overall cost of energy Reduction

## Work Package WP3 Controls and Operational Strategy

### Deliverable D3.2 Control Simulation Model for X-Rotor Concept

*Funding Instrument:* Innovation Action  
*Call:* H2020-LC-SC3-2018-2019-2020  
*Call Topic:* LC-SC3-RES-1-2019-2020

*Project Start:* 1 January 2021  
*Project Duration:* 36 months

*Beneficiary in Charge:* University of Strathclyde

Dissemination Level		
PU	Public	✓
PP	Restricted to other programme participants (including the Commission Services)	
RE	Restricted to a group specified by the Consortium (including the Commission Services)	
CO	Confidential, only for members of the Consortium (including the Commission Services)	

## Deliverable Information

Document Administrative Information	
Project Acronym:	XROTOR
Project Number:	101007135
Deliverable Number:	D3.2
Deliverable Full Title:	Control Simulation Model for X-Rotor Concept
Deliverable Short Title:	XROTOR Control Model
Document Identifier:	XROTOR-D32-XROTORControlModel-draft-v1.1
Beneficiary in Charge:	University of Strathclyde
Report Version:	v1.1
Contractual Date:	31/03/2022
Report Submission Date:	31/03/2022
Dissemination Level:	PU
Nature:	Report
Lead Author(s):	Laurence Morgan (University of Strathclyde)
Co-author(s):	Adam Stock (University of Strathclyde), W.E. Leithead (University of Strathclyde)
Keywords:	Control Model, Aerodynamics, Wind Model
Status:	<u>x</u> draft, <u>_</u> final, <u>_</u> submitted

## Document information

Date	Version	Author/Editor	Summary of Changes Made
29/09/2021	v1.0	W.E. Leithead (University of Strathclyde)	Draft version of the report

# Table of Contents

Executive Summary .....	11
1. Deliverable details .....	12
2. Introduction to the X-Rotor Concept .....	13
3. Control Model.....	14
3.1 Effective Wind Speed Modelling .....	14
3.2 Primary Rotor Modelling .....	19
3.3 Power Take-Off Modelling .....	34
4. Simulation Outputs .....	37
4.1 Model Parameterisation.....	37
4.2 Control model outputs with uniform wind speed. ....	38
4.3 Control model outputs with wind speed ramp .....	43
4.4 Effective of aerodynamic damping on primary rotor power tracking .....	46
4.5 Model outputs with effective wind speed model .....	48
5. Conclusions .....	52
References .....	53
Appendix A - Secondary rotor design .....	54

## List of Figures

Figure 1: Concept drawing of the X-Rotor .....	13
Figure 2: 'True' X-Shaped X-Rotor.....	16
Figure 3: Mapping 'true' X-Shape to the X-Rotor .....	18
Figure 4: Discretisation procedure used for DMS simulations.....	23
Figure 5: The streamtube and blade element geometries used in the DMS method .....	24
Figure 6: Comparison of the rotor power coefficient as simulated using the base DMS model and the Base LLT model.....	27
Figure 7: Comparison of the variation in torque coefficient as simulated using the base DMS model and the Base LLT model.....	28
Figure 8: Comparison of the rotor power coefficient as simulated using the fully corrected DMS model and the fully corrected LLT model .....	29
Figure 9: Comparison of the variation in torque coefficient as simulated using the fully corrected DMS model and the fully corrected LLT model .....	30
Figure 10: Upper blade torque coefficient $M_\theta$ presented on the $\lambda, \theta$ plane over a range of pitch offsets. ....	31
Figure 11: Lower blade torque coefficient $M_\theta$ presented on the $\lambda, \theta$ plane .....	32
Figure 12: Upper blade radial flapwise moment coefficient $M_\phi$ presented on the $\lambda, \theta$ plane over a range of pitch offsets. ....	33
Figure 13: Torque and thrust coefficient comparison between QBlade and FAST(Aerodyn).....	35
Figure 14: Torque and thrust coefficient for the secondary rotors.....	36
Figure 15: X-Rotor power tracking in a uniform wind speed of 12.5m/s. ....	40
Figure 16: X-Rotor loads in a uniform wind speed of 12.5m/s.....	41
Figure 17: X-Rotor structural deflections in a uniform wind speed of 12.5m/s. ....	42
Figure 18: X-Rotor power tracking response to a steady change in wind speed from 3m/s to 12.5m/s	43
Figure 19: X-Rotor loading in response to a steady change in wind speed from 3m/s to 12.5m/s.....	44
Figure 20: X-Rotor structural deflections in response to a steady change in wind speed from 3m/s to 12.5m/s .....	45
Figure 21: Caption.....	47
Figure 22: Power tracking response for the X-Rotor simulated with an effective wind speed model with a mean wind speed of 12.5m/s .....	49
Figure 23: X-Rotor loads simulated with an effective wind speed model with a mean wind speed of 12.5m/s .....	50
Figure 24: X-Rotor structural response simulated with an effective wind speed model with a mean wind speed of 12.5m/s .....	51
Figure 25: Secondary rotor chord and twist distribution .....	56

# List of Tables

Table 1: Primary rotor variables given in previous reports ..... 37  
Table 2: X-Rotor simulation variables derived using representative assumptions. .... 39  
Table 3: Secondary rotor parameters for control model. .... 39

# Nomenclature

$\alpha'$	Streamline curvature corrected angle of attack
$\alpha_{[u/d]}$	Upwind/Downwind angle of attack
$\alpha_{design}$	Design angle of attack
$\alpha_{dyn}$	Dynamic angle of attack
$\alpha_{ss}$	Static stall angle
$\beta$	Blade pitch angle
$\Delta\phi_{Bl}$	Difference between lower blade vertical angle and attachment angle
$\Delta\phi_{Bu}$	Difference between upper blade vertical angle and attachment angle
$\Delta\theta_{Bl}$	Difference between lower blade and hub angle of azimuth
$\Delta\theta_{Bu}$	Difference between upper blade and hub angle of azimuth
$\eta_a$	Aerodynamic efficiency
$\eta_g$	Generator efficiency
$\gamma_{el}$	Upper blade edgewise damping constant
$\gamma_{eu}$	Upper blade edgewise damping constant
$\gamma_{fl}$	Lower blade flapwise damping constant
$\gamma_{fu}$	Upper blade flapwise damping constant
$\Lambda$	Non-dimensional lift distribution
$\lambda$	Primary rotor tip speed ratio
$\lambda_s$	Secondary rotor tip speed ratio
<b>R</b>	Rotation matrix
$\mu$	Damping ratio
$\omega$	Primary rotor rotor speed
$\omega_s$	Secondary rotor rotor speed
$\omega_{el}$	1st lower blade edgewise frequency
$\omega_{eu}$	1st upper blade edgewise frequency
$\omega_{fl}$	1st lower blade flapwise frequency

$\omega_{fu}$	1st upper blade flapwise frequency
$\omega_{g0}$	Minimum generator frequency at rated power
$\omega_g$	Generator speed
$\phi_{Bl}$	Lower blade vertical angle
$\phi_{Bu}$	Upper blade vertical angle
$\psi_l$	Lower blade vertical attachment angle
$\psi_u$	Upper blade vertical attachment angle
$\rho$	Air density
$\rho_{Lc}$	Mass per unit length of the rotor cross arm
$\Theta$	Blade angle
$\theta$	Angle of azimuth
$\theta_{Bl}$	Lower blade angle of azimuth
$\theta_{Bu}$	Upper blade angle of azimuth
$\tilde{J}_{Bl}$	Effective lower blade inertia
$\tilde{J}_{Bu}$	Upper blade additional effective centrifugal inertia
$\tilde{J}_{lu}$	Lower blade additional effective centrifugal inertia
$\Upsilon$	Equivalent horizontal axis azimuth for 'true' X approximation
$\xi$	Relative aerofoil attachment point
$\zeta_{[u/d]}$	Upwind/Downwind expansion factor
$A_l$	Lower rotor area
$A_M$	Masse's dynamic stall interpolation coefficient
$A_P$	Primary rotor area
$A_s$	Secondary rotor area
$a_s$	Secondary rotor axial induction factor
$a_T$	Turbulent wake transition induction factor
$A_u$	Upper rotor area
$a_{[u/d]}$	Upwind/Downwind induction factor
$a_{ts}$	Secondary rotor tangential induction factor
$c$	Blade chord length
$c_c$	Crossarm chord
$C_D$	Drag coefficient
$C_L$	Lift coefficient
$C_P$	Power coefficient

$C_{[L/D]_{dyn}}$	Dynamic lift/drag coefficient
$C_{[L/D]_{static}}$	Static lift/drag coefficient
$C_{\phi l}$	Lower rotor radial flapwise bending moment coefficient
$C_{\phi u}$	Upper rotor radial flapwise bending moment coefficient
$C_{Dc}$	Crossarm drag coefficient
$C_{L_{design}}$	Design lift coefficient
$C_n$	Normal force coefficient
$C_{PP}$	Primary rotor power coefficient
$C_{Ps}$	Secondary rotor power coefficient
$C_{Ql}$	Lower rotor torque coefficient
$C_{Qs}$	Secondary rotor torque coefficient
$C_{Qu}$	Upper rotor torque coefficient
$C_{TBE[u/d]}$	Upwind/Downwind thrust coefficient from blade element theory
$C_{TM[u/d]}$	Upwind/Downwind thrust coefficient from fluid momentum theory
$C_{Ts}$	Secondary rotor thrust
$C_t$	Tangential force coefficient
$d$	Tip loss disk spacing
$D_Q$	Local torque contribution
$D_R$	Local radial flapwise bending moment contribution
$F$	Tip loss factor
$f$	local angular displacement as a fraction of blade tip angular displacement
$F_h$	Tip loss function for horizontal axis turbines
$g$	gravitational acceleration
$J_c$	Cross-arm inertia
$J_H$	Effective hub inertia
$J_s$	Secondary rotor inertia
$J_{Bu}$	Effective upper blade inertia
$J_g$	Generator inertia
$J_{Hb}$	Blade to contribution to effective hub inertia
$k$	Glide ratio
$k_c$	Secondary rotor controller constant
$K_e$	Electrical stiffness
$K_s$	Shaft stiffness

$k_{design}$	Design glide ratio
$l$	Blade length
$l_{Blcm}$	Spanwise location of lower blade centre of mass
$l_{Bucm}$	Spanwise location of upper blade centre of mass
$l_c$	Crossarm radius
$m_B$	Blade mass
$M_{\phi l}$	Lower blade root radial flapwise bending moment
$M_{\phi u}$	Upper blade root radial flapwise bending moment
$M_{\theta l}$	Lower blade aerodynamic torque
$M_{\theta s}$	Secondary aerodynamic torque
$M_{\theta u}$	Upper blade aerodynamic torque
$m_{Bl}$	Lower blade mass
$m_{Bu}$	Upper blade mass
$m_s$	Secondary rotor mass
$N$	Blade number
$p$	Number of pole pairs
$P_P$	Primary rotor power
$P_S$	Secondary rotor power
$P_g$	Generator power
$Q_{RG}$	Shaft torque
$Q_C$	Crossarm parasitic torque contribution
$Q_U$	Blade torque contribution
$r$	Radial coordinate
$R_c$	Crossarm radius
$R_l$	Lower rotor radius
$R_P$	Primary rotor radius
$R_s$	Secondary rotor radius
$R_u$	Upper rotor radius
$R_{sh}$	Secondary rotor hub radius
$s$	Spanwise blade coordinate
$t$	Aerofoil thickness
$T_s$	Secondary rotor thrust
$U_M$	Maximum allowable tip speed

$U_R$	Rated wind speed
$U_s$	Secondary rotor incident wind speed
$U_{a[u/d]}$	Upwind/Downwind apparent velocity
$U_{I[u/d]}$	Upwind/Downwind incident velocity
$U_{N[u/d]}$	Upwind/Downwind no-load velocity

# Executive Summary

## Deliverable Description

This deliverable report supports deliverable D3.1 '*Control Simulation Model of X-Rotor Concept*', and details the design and development of a control model for the X-Rotor concept, which aims to provide a transparent tool for prototyping controller designs, to support controller analysis and design and to assess the effectiveness of controllers in meeting design objectives.

## Responsible Partner

The responsible partner is the University of Strathclyde, with Prof. W.E. Leithead as the principle investigator.

## Deliverable Outcomes

A control model of the X-Rotor concept, suitable for prototyping controller designs, supporting controller analysis and design and assessing the effectiveness of controllers in meeting design objectives is presented. The complexity of the model is minimised whilst retaining sufficient detail to capture the essential dynamic properties. The model is designed using MATLAB/Simulink.

The control model consists of three main components, the wind model, the primary rotor aerodynamics and structural dynamics and the power take-off (including secondary rotor dynamics).

The wind model is adapted from that described in (Gala Santos, 2018), and consists of an effective wind field that contains appropriate frequency components up to six times the rotational frequency of the primary rotor.

The primary rotor aerodynamics use the outputs from a bespoke double multiple streamtube (DMS) model (validated against the higher fidelity 'CACTUS' lifting line model) to populate a look-up table approach. The outputs of the DMS model and its validation against the CACTUS model are presented. The primary rotor structural model includes compliant upper blade dynamics and semi-compliant lower blade dynamics.

The power take-off dynamics include modelling of the secondary rotors using an actuator disc model. The model is validated against the BEM tool 'QBlade'. The power train of the power take-off is modelled as a semi-compliant shaft connected to a direct drive generator.

Illustrative simulation results are presented that show that the essential dynamic properties of the X-Rotor concept are simulated within the control model.

# 1 Deliverable details

This report supports deliverable *D3.1 Control Simulation Model of X-Rotor Concept*.

The purpose of the control simulation model for the X-rotor concept is to provide a transparent tool for prototyping controller designs, to support controller analysis and design and to assess the effectiveness of controllers in meeting design objectives. The complexity of the control simulation should be kept to a minimum whilst capturing all essential dynamic properties. Such a simulation model for the X-rotor concept has been constructed using MATLAB/Simulink.

The control model consists of the following distinct parts:

1. X-Rotor Wind Speed Model
2. Primary Rotor: Aerodynamics and Rotor Dynamics
3. Power Take-Off Dynamics: Secondary Rotor Aerodynamics and Rotor Dynamics

This deliverable report gives details of each part of the X-Rotor model in turn prior to results and discussion of a set of example simulation outputs. The simulation results in the report are for an illustrative choice of parameters only. These will be updated using future outcomes from WP2, WP4 and WP5.

In **section 2** an overview of the X-Rotor concept is presented. In **section 3** the control model is described in detail, with sub-sections focusing on each of the sub-models within it. The results of simulations are presented and discussed in **section 4**, before conclusions are drawn in **section 5**.

## 2 Introduction to the X-Rotor Concept

The X-Rotor Concept is described in Leithead 2019 (Leithead, Camciuc, Amiri, & Carroll, 2019). It consists of a highly modified double-V-Rotor, with a traditional upper V, and an inverted lower V which increases the potential for power capture and cancels the overturning moments inherent in the traditional V-Rotor design. This primary rotor is freely mounted on a central tower disconnected to any drive-train and the power-take-off is performed by compact secondary rotors attached to the outer edge of the inverted lower V. A concept drawing is provided in figure 1.

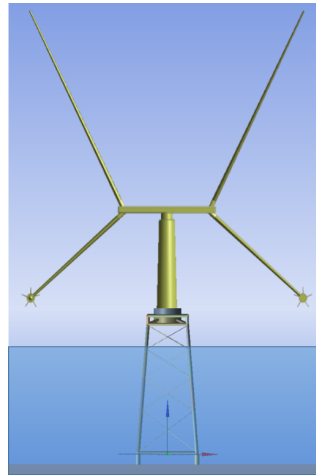


Figure 1: Concept drawing of the X-Rotor

The design challenge for the primary rotor of the X-Rotor can be considered as somewhat similar to the design challenge for a traditional VAWT. V-Rotor configurations have the potential to maximise power per unit weight of a rotor through the maximisation of the rotor swept area, however they intrinsically suffer from large overturning moments. These have previously been compensated for by the use of aerodynamic sails; perpendicularly attached secondary blades which provide an opposing force contribution, effectively cancelling out the overturning moments. In the case of the X-Rotor, rather than attaching aerodynamic sails, the use of a secondary lower rotor half has been proposed as it can simultaneously perform three beneficial functions:

- Increase the primary rotor swept area thus increasing power capture.
- Support the secondary rotors.
- Oppose the rotor overturning moment.

The secondary rotors are supported off of the blade tips of the lower rotor half, this provides two key benefits. Firstly, by attaching the secondary rotors at the maximum possible radius, it is ensured that they see the highest possible relative wind-speeds, increasing the effective power density allowing for rotors with smaller radius and an increased rotational speed. This allows the secondary rotor drive-train to forego a gearbox. Secondly, it situates the secondary rotors as close as possible to the ocean surface, which facilitates lower operations and maintenance costs, as large heavy lift vessels are not required to work on the secondary rotor. A preliminary optimisation of the primary rotor design, considering both aerodynamic performance and structural limitations has been completed and the results are given in Leithead 2019 (Leithead et al., 2019).

## 3 Control Model

Control models are used by control engineers to design controllers for devices. The requirements of a control model differ dependent upon the device being modelled, however, for a wind turbine, the requirements are that the model must represent the fundamental dynamics of the turbine that are relevant to controller design. For the X-Rotor, the fundamental dynamics are,

1. The wind field input
2. The primary rotor aerodynamics and structural dynamics
3. The power take-off dynamics (including the secondary rotor dynamics)

Control models are used to design controllers that can then be more fully tested on more detailed, higher fidelity models. As such, control models for wind turbines typically require just the first structural mode for the structural dynamics and simple representations of the electrical components of the system. Computational efficiency is a key requirement of a control model, as controller design is often an iterative process, requiring many simulations to test controller designs. If the control model is not computationally efficient and is therefore slow to run, then the controller design process is severely impacted.

The X-Rotor control model uses an effective wind speed as an input to the system. The effective wind speed is a heavily adapted form of the effective wind field model described in (Gala Santos, 2018). A description of the effective wind field model including the adaptations made for the X-Rotor case are described in sub-section 3.1.

The primary rotor dynamics are modelled using a rigid hub and two-lumped inertia blade models with semi compliant (1 degree of freedom) lower blades and fully compliant (2 degrees of freedom) upper blades, this approach is adapted from (Leithead, 2020) and is described in sub-section 3.2.1. The primary rotor aerodynamics are obtained from a bespoke double multiple streamtube model based on the work in (Sharpe & Freris, 1990) which is described and validated in sub-section 3.2.2.

The power take off modelling is described in sub-section 3.3.

### 3.1 Effective Wind Speed Modelling

Horizontal Axis Wind Turbines (HAWTs) have made use of effective wind speed models for many years. The effective wind speed is intended to only represent the low frequency variations in the wind (lower than the rotational frequency of the turbine).

#### 3.1.1 Rotational Sampling of the Wind - Effective Wind Field Model

For horizontal axis wind turbines, it is possible to build an effective wind-field model that is suitable for control purposes, which includes components that induce the correct torque on each blade and the thrust on the tower with the correct correlations over the frequency range up to 6P (Gala Santos, 2018). Once sampled (as opposed to prior to sampling), the structure of the proposed wind-field model can be thought of as a number of sinusoids of different frequencies and amplitudes that sum to form a more complex signal in a manner analogous to a Fourier series. It is worth noting that, for the wind-field model, the frequency, amplitude and phase are

varying continuously for all the individual components in a random manner. In this way, the *wind field* is modelled rather than a *wind speed*.

The derivation of the wind field model is complex and is described in detail in (Gala Santos, 2018). Suffice it to say that the model has the form,

$$\begin{aligned} V_{uniform}(t) &= a_{nUniform}(t) \cos n\Upsilon + b_{nUniform}(t) \sin n\Upsilon \\ V_{linear}(t) &= a_{nLinear}(t) \cos n\Upsilon + b_{nLinear}(t) \sin n\Upsilon \end{aligned} \quad (1)$$

where  $\Upsilon$  is the azimuth angle of the rotor<sup>1</sup>.

The 'uniform' subscript refers to the components that, once sampled, result in forces (which are independent of the position on the blade on which they act), whilst the 'linear' subscript refers to components that, once sampled, result in torques or moments (which are linearly proportional to the distance from the rotor hub). Hence, for  $m$  periodic components, the wind model can be written as,

$$V(\Upsilon, t) = \hat{V} + V_0(t) + \sum_m \left[ (a_m(t)) \cos(m\Upsilon) + (b_m(t)) \sin(m\Upsilon) \right] \quad (2)$$

where  $V_0(t)$  is the low frequency changes in effective wind speed across the whole rotor,  $\hat{V}$  is the quasi-static wind speed and  $m$  is the integer periodic component. Note that the wind speed used to calculate induced moments and torques uses different values of  $a_m(t)$  and  $b_m(t)$  to those used by the wind speed to calculate forces. For ease of notation, this distinction is neglected in the following descriptions (but not in the model).

### 3.1.2 Adaptation of the Wind Model for the X-Rotor Case

Thus far the effective wind speed and wind field models have pertained to HAWTs rather than the X-Rotor primary rotor. In the models discussed, only the wind speed perpendicular to the HAWT's (vertical) rotor disc has been considered. For a HAWT rotor it is typical to use these effective wind models with aerodynamic coefficient models to determine the forces and torques acting on the disc. The moments and forces on a blade can also be inferred through the modelling described briefly in section 3.1.1 and more fully in (Gala Santos, 2018). The wind speed for the low frequency models is described by the relationship,

$$V(t) = \bar{V} + V_e(t) \quad (3)$$

whereby  $V_e(t)$  is a time varying wind speed that is uniform over the disc. It represents the wind speed components that can be considered as quasi-static over a whole rotor revolution - that is over frequencies lower than 1P. Similarly, an effective wind field model is described in section 3.1.1 whereby,

$$V(\Upsilon, t) = \hat{V} + V_0(t) + \sum_m \left[ (a_m(t)) \cos(m\Upsilon) + (b_m(t)) \sin(m\Upsilon) \right] \quad (4)$$

where  $\Upsilon$  is the disc azimuth angle. The wind field model represents wind components across a broader range than the wind speed model, with the latter limited to frequencies below 1P,

<sup>1</sup>Note that  $\Upsilon$  is used instead of the more common  $\theta$  in this report to avoid confusion with the azimuth of the X-Rotor primary rotor

whilst the former includes frequencies up to  $6P$ . An effective wind speed for a blade is obtained by substituting the azimuthal angle for the blade  $\Upsilon_B$  for  $\Upsilon$  in equation 4. The model provides appropriately correlated linearly and uniformly weighted wind speeds suitable for calculating moments/torques and forces respectively. When effective wind speeds for a number of blades rotating in the disc are obtained, these too are appropriately correlated. Appropriate load  $nP$  components are thereby induced.

In the case of the X-Rotor primary rotor, the rotor rotates about a different axis. However, through the assumptions and re-working of the model explained in this section, the HAWT effective wind speed model can be used as a reasonable approximation for the X-Rotor primary rotor effective wind speed.

First, let us consider a 'true' X-Rotor, that is a rotor with the shape of a capital X as shown in Figure 2a).

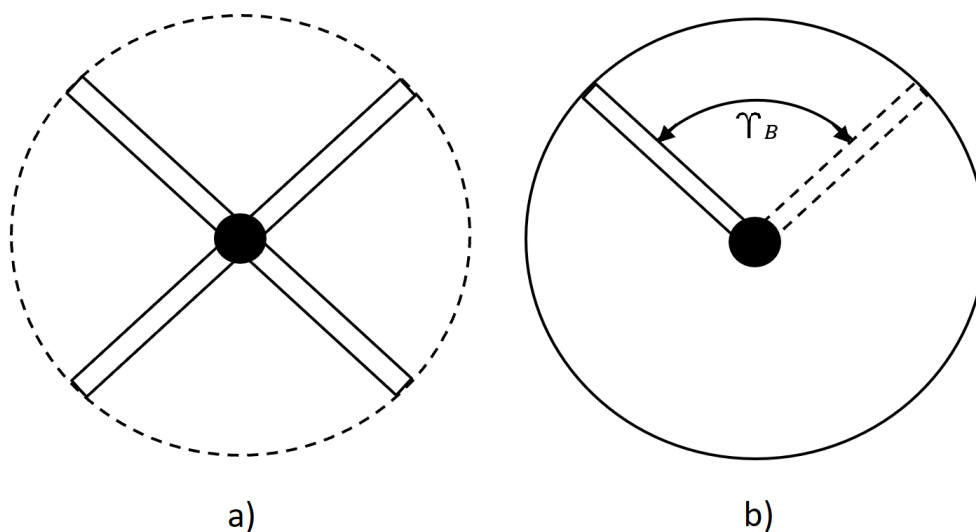


Figure 2: 'True' X-Shaped X-Rotor

As the rotor rotates about the vertical axis, each blade can be thought of as sweeping from one side to another as shown in Figure 2b), whilst pitching forwards and backwards (into and out of the page) at a frequency of  $1P$  with an amplitude of  $\psi$ , where  $\psi$  is the angle of each blade in the X shape in Figure 2, measured relative to a vertical line. Hence, a cone shape is swept out by each blade.

Ignoring the pitching of the rotor disc for now, an effective wind speed is obtained by substituting the blade angle  $\Upsilon_B$  from Figure 2b) into equation 4. The wind field model can be viewed as a cylinder, with radius of the blade length and longitudinal axis time. The value of the wind speed at any point in the cylinder defined by  $(r, \Upsilon, t)$  is  $V(\Upsilon, t)$  as defined by the wind field model in equation 4.

Assuming the wind field is homogeneous, an underlying assumption in the derivation of the wind models, the wind field model of equation 4 remains valid, albeit for wind speeds that are no longer perpendicular to the disc, with  $\Upsilon$  remaining the disc azimuth angle. Considering the 'pitching' of the rotor disc, so long as a blade lying on a tilted disc rotates sufficiently slowly that  $\Upsilon_B$  can be considered quasi-static, then the effective wind speed for that blade is obtained as before (i.e. by substituting  $\Upsilon_B$  into equation 4). Since the aerodynamic coefficients are derived on the basis of a horizontal wind speed uniform over the rotor, the impact of wind speed not

being perpendicular to the disc would be incorporated by the aerodynamic coefficients.

However, if  $\Upsilon_B$  cannot be considered quasi-static, the frequencies of wind turbulence are essentially compressed when the blade moves into the wind and extended when the blade moves out of the wind. This aspect of the rotor/wind field interaction is not accounted for in the wind field model as described thus far. This drawback of the wind field model can be avoided as described below.

The wind field is defined with reference to a particular mean wind speed  $\bar{V}$ , and so the longitudinal axis can be relabelled in terms of a distance  $d$  where  $d = \bar{V}t$ , assuming a frozen 3D turbulence model.

Consider a rotor with several blades rotating about a common axis in a disc perpendicular to the wind but displaced from each other in the direction of the wind. By moving the discs containing each blade through the frozen 3D representation, the effective wind speeds for each blade are obtained as,

$$\begin{aligned}\tilde{V}(\Upsilon_B, t) &= V(\Upsilon_B, t - d/\bar{V}) \\ &= \bar{V} + V_0(t - d/\bar{V}) + \sum_m \left[ (a_m(t - d/\bar{V}))\cos(m\Upsilon_B) \right. \\ &\quad \left. + (b_m(t - d/\bar{V}))\sin(m\Upsilon_B) \right]\end{aligned}\quad (5)$$

with the values of  $\theta_B$  and  $d$  chosen to be those for each blade (note that  $d$  is the downstream displacement relative to the furthest upstream blade). The displacement  $d$  need not be constant, it can vary with time. Whilst the auto-covariances are unchanged as required, the cross-covariances between blades are changed by the introduction of the displacements. As well as introducing frequency compression and extension when the blade moves relative to the wind speed, the correlation of the effective wind speeds for blades rotating in discs that are displaced from each other is reduced as required.

The effective wind speed described in equation 5, can be extended to the situation for which the displacement of the blade from the vertical disc is not, as is the case with the blade lying in a disc tilted about its horizontal diameter, constant over the blade. The displacement could be that for a representative point on the blade, such that the correlation with the effective wind speed for the corresponding point on the vertical disc is reduced as appropriate. A 4-bladed vertical axis rotor with an X-shaped geometry is depicted in Figure 2a). (The coning angle for the upper and lower halves need not be the same.) Aerodynamically, the most important part of the blade is outer part. Taking this into consideration, the representative point for a blade is towards the tip, say, at a distance  $\delta R$  from the hub. A reasonable choice for  $\delta$  would be 2/3. The effective wind speed for a blade is equation 5 with,

$$\Upsilon_B = \tan^{-1}(\sin(\theta)\tan(\psi)) \quad (6)$$

where  $d = \delta R \cos(\theta) \sin(\psi)$ , where  $\theta$  is the angle of rotation of the blade (when the blade is upwind lying in a vertical plane parallel to wind speed,  $\theta$  is defined to be  $0^\circ$ ) and  $d$  is the displacement relative to the vertical disc.

In the X-rotor concept the geometry of the primary rotor differs from the ‘true’ X shape depicted in Figure 2. However, the impact of the difference in geometry is reduced by it being less for the outer part of the blades, which contribute to effective wind speeds with greater weighting than the inner part. The pragmatic choice for the effective wind field remains equation 5 with its parameters set for an equivalent rotor with the geometry in Figure 2. Since control models are not required to have high fidelity, this pragmatic choice of effective wind speeds for the

X-rotor concept and the rather less pragmatic choice for a 4-bladed vertical axis rotor with an X-shaped geometry should suffice for control design purposes. Figure 3a) depicts the rotor geometry of the X-rotor, in black, and the geometry of the equivalent vertical axis wind turbine with an X-shaped rotor, in red. The length of the blades for the latter is,

$$l_r = \sqrt{l^2/4 + (l_u \sin(\psi_u - \kappa) + l_c \sin(\kappa)/2)^2} \quad (7)$$

where,

$$l = \sqrt{l_u^2 + l_l^2 - 2l_u l_l \sin(\psi_l - \psi_u)} \quad (8)$$

$$\kappa = \arcsin(2(l_u \sin \psi_u - l_l \sin \psi_l)/l)$$

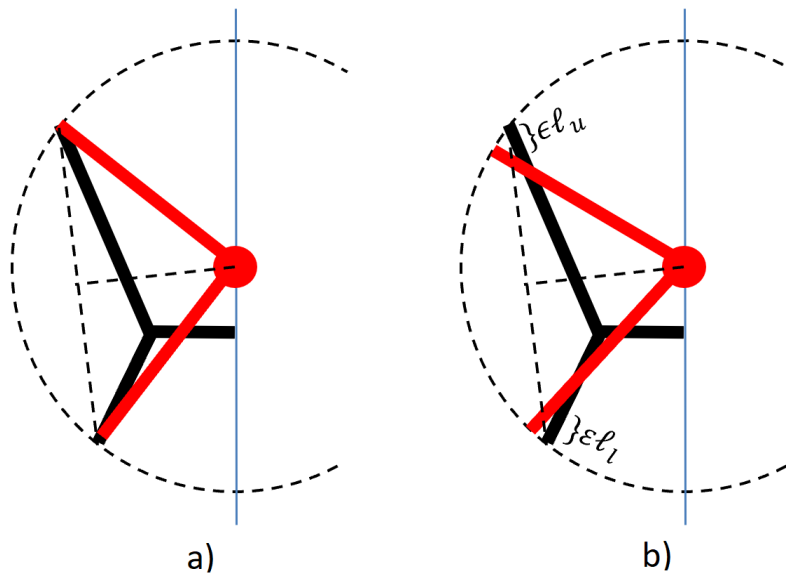


Figure 3: Mapping 'true' X-Shape to the X-Rotor

A correction to the equivalent rotor to reduce the difference in geometry of the outer part of the blades is shown in Figure 3b). The corrections to  $\psi_u$  and  $\psi_l$  are, respectively,

$$\arctan(\epsilon_{l_u} \sin(\Delta\psi_u)/(l_r - \epsilon_{l_u} \cos(\Delta\psi_u))) \quad (9)$$

$$\arctan(\epsilon_{l_l} \sin(\Delta\psi_l)/(l_r - \epsilon_{l_l} \cos(\Delta\psi_l)))$$

A reasonable choice for  $\epsilon$  is 1/6.

The wind-field model (equation 5), for the equivalent rotor in Figure 3b) and geometry defined by equation 7 (including the corrections in equation 9) remains appropriate for the X-rotor provided  $\Upsilon$  is the solution of equation 5.

### 3.1.3 Effective Wind Speeds for Secondary Rotors

The secondary rotors are HAWTs and, as such, the effective wind speed discussed in section ?? can be utilised. Of course, there is still some coherence between the wind field experienced by the primary rotor and the effective wind speed interacting with the secondary rotor. Note

that due to the high speed of rotation of the secondary rotor and the corresponding high frequency of the nP components, these nP components can be ignored for the control model as their frequencies will be an order of magnitude higher than the dominant mechanical frequencies.

The swept area of the primary and secondary rotors are significantly different, which must be accounted for in the effective wind speeds used. The effective wind speed component,  $V_e(t)$ , in equation 3 is obtained by filtering a point wind speed with zero mean. Let  $H_P(s)$  and  $H_S(s)$  be this filter for the primary rotor and secondary rotors, respectively. The bandwidth of  $H_P(s)$  is much less than the bandwidth of  $H_S(s)$  due to the differing size of the effective swept area.

An appropriate effective wind speed for a secondary rotor is,

$$\bar{V} + V_e(t) + \tilde{V}_e(t) \quad (10)$$

where  $\tilde{V}_e(t)$  is obtained by filtering a point wind speed with zero mean by  $H(s)$  such that,

$$H(s)H(-s) = H_S(s)H_S(-s) - H_P(s)H_P(-s) \quad (11)$$

The point wind speed for  $\tilde{V}_e(t)$  is generated using a white noise independent from that used to generate  $V_e(t)$ . The effective wind speed for the secondary rotors are then

$$V_{S1} = R_P \Omega_P - (\bar{V} + V_e(t) + \tilde{V}_{e1}(t)) \sin(\theta_P) \quad (12)$$

and

$$V_{S2} = R_P \Omega_P - (\bar{V} + V_e(t) + \tilde{V}_{e2}(t)) \sin(\theta_P - \pi) \quad (13)$$

When the effective wind speed is obtained using equation 4, a similar approach is adopted with  $V_0(t)$  replacing  $V_e(t)$  in the above expressions.

## 3.2 Primary Rotor Modelling

The primary rotor is modelled in two separate stages, the rotor dynamics and the rotor aerodynamics, with the latter acting as an input to the former.

### 3.2.1 Primary Rotor Dynamics

#### Overview of approach

The primary rotor dynamics can first be considered using a two-lumped inertia model described in (Leithead, 2020). Here, each blade is modelled with two degrees of freedom,  $\theta$  and  $\phi$ , corresponding to the azimuthal motion and radial flapping motion respectively, whilst the hub is considered a stiff beam with only one degree of freedom in the azimuthal plane,  $\theta$ . The two lumped inertia model splits the inertia of the blade between the effective contribution to the hub inertia,  $J_{Hb}$  and the effective blade inertia relative to the hub,  $J_B$ . The effective hub inertia is given by the sum of each of the effective blade inertia contributions and the inertia of the cross arm,  $J_c$ :

$$J_H = J_c + \sum_i J_{Hb}^{[i]} \quad (14)$$

The effective blade inertia and the effective hub inertia contribution are given by:

$$J_{Hb} = J_{Bt} - \frac{B^2}{C} \text{ and } J_B = \frac{B^2}{C}, \quad (15)$$

where the constants  $J_{Bt}$ ,  $B$  and  $C$  are given by

$$J_{Bt} = \int_0^R m_B(r)r^2 dr, \quad B = \int_0^R m_B(r)r^2 f(r) dr \quad \text{and} \quad C = \int_0^R m_B(r)r^2 f(r)^2 dr. \quad (16)$$

Here  $f(r)$  represents local angular displacement as a fraction of the angular displacement at the blade tip for a given mode and  $m_B(r)$  represents the mass distribution along the blade. With the effective hub and blade inertias defined, the dynamics of the blades and hub can be derived individually.

### Blade Dynamics

The blade dynamics can be further simplified through the assumption that the blade is roughly cylindrical. This implies that the inertia associated with flapwise and edgewise motion can be taken as identical, allowing the blade inertia to be represented by a scalar value. Under these assumptions the upper blade dynamics are described with

$$J_{Bu} \begin{bmatrix} \ddot{\theta}_{Bu} \\ \ddot{\phi}_{Bu} \end{bmatrix} = -J_{Bu} \mathbf{R}(\beta) \begin{bmatrix} \omega_{eu}^2 & 0 \\ 0 & \omega_{fu}^2 \end{bmatrix} \mathbf{R}^{-1}(\beta) \begin{bmatrix} \Delta\theta_{Bu} \\ \Delta\phi_{Bu} \end{bmatrix} - J_{Bu} \mathbf{R}(\beta) \begin{bmatrix} \gamma_{eu} & 0 \\ 0 & \gamma_{fu} \end{bmatrix} \mathbf{R}^{-1}(\beta) \begin{bmatrix} \Delta\dot{\theta}_{Bu} \\ \dot{\phi}_{Bu} \end{bmatrix} \quad (17)$$

$$+ \begin{bmatrix} M_{\theta u}(\theta, \beta, U_0, \dot{\theta}) \\ M_{\phi u}(\theta, \beta, U_0, \dot{\theta}) \end{bmatrix} + \begin{bmatrix} 0 \\ (J_{Bu} + \tilde{J}_{Bu})\dot{\theta}_{Bu}^2 \cos(\phi_{Bu}) + gm_{Bu}l_{Bucm} \sin(\phi_{Bu}) \end{bmatrix}$$

where  $J_{Bu}$  represents the effective upper blade inertia relative to the hub,  $\omega_{eu}$  and  $\omega_{fu}$  represent the first upper blade flapwise and edgewise frequencies,  $\mathbf{R}$  represents the rotation matrix,  $\beta$  the blade pitch angle,  $\Delta\theta_{Bu}$  the difference between the blade and hub angle of azimuth,  $\Delta\phi$ , the difference between blade radial inclination angle and the attachment angle,  $\gamma_{eu}$  and  $\gamma_{fu}$  the upper blade edgewise and flapwise damping constants,  $\Delta\dot{\theta}_{Bu}$  the difference between the angular speed of upper blade and the hub,  $M_{\theta}$  and  $M_{\phi}$  the aerodynamic torques in the azimuthal and radial flapwise directions,  $U_0$  the effective wind speed,  $g$  gravitational acceleration,  $m_{Bu}$  the upper blade mass,  $l_{Bucm}$  the spanwise location of the upper blade center of mass and  $\tilde{J}_{Bu}$  the additional inertia associated with centrifugal motion given by

$$\tilde{J}_{Bu} = m_{Bu}(l_c^2 + 2l_c l_{Bucm} \sin(\phi_{Bu}) - l_c^2 \sin^2(\phi_{Bu})). \quad (18)$$

Similarly, the lower blade dynamics are governed by

$$J'_{Bl} \begin{bmatrix} \ddot{\theta}_{Bl} \\ \ddot{\phi}_{Bl} \end{bmatrix} = -J'_{Bl} \begin{bmatrix} \omega_{el}^2 & 0 \\ 0 & \omega_{fl}^2 \end{bmatrix} \begin{bmatrix} \Delta\theta_{Bl} \\ \Delta\phi_{Bl} \end{bmatrix} - J'_{Bl} \begin{bmatrix} \gamma_{el} & 0 \\ 0 & \gamma_{fl} \end{bmatrix} \begin{bmatrix} \Delta\dot{\theta}_{Bl} \\ \dot{\phi}_{Bl} \end{bmatrix} \quad (19)$$

$$+ \begin{bmatrix} M_{\theta l}(\theta, \dot{\theta}, U_0) \\ M_{\phi l}(\theta, \dot{\theta}, U_0) \end{bmatrix} + \begin{bmatrix} 0 \\ (J_{Bl} + \tilde{J}_{Bl})\dot{\theta}_{Bl}^2 \cos(\phi_{Bl}) + gm_{Bl}l_{Blcm} \sin(\phi_{Bl}) \end{bmatrix}$$

$$+ \begin{bmatrix} -T_s(l_{Bl} \sin(\phi_{Bl}) + l_c) \\ l_{Bl} m_{Sr} g \sin(\phi_{Bl}) + \{l_c + l_{Bl} \cos(\phi_{Bl})\} m_{Sr} \dot{\theta}_{Bl}^2 l_{Bl} \cos(\phi_{Bl}) \end{bmatrix}.$$

Here, the first terms are identical to the upper blade dynamics however the pitch angle is fixed at  $\beta = 0$  and the subscripts  $u$  are substituted for the subscripts  $l$  to denote lower blade values. An additional term is also included to represent the aerodynamic, gravitational and centrifugal forces imparted by secondary rotor. Here  $T_s$  represents the thrust force from the secondary rotor and  $m_{Sr}$  represents the mass of the secondary rotor. In addition to this, the inertia of the lower blade must be modified from the definition given in equation 15 to include the inertia due to the secondary rotor such that

$$J'_{Bl} = J_{Bl} + m_{Sr}(l_c + l_{Bl} \sin(\phi_{Bl}))^2 \approx J_{Bl} + m_{Sr}(l_c + l_{Bl} \sin(\psi_l))^2. \quad (20)$$

As the combined effect of the centrifugal and gravitational forces from the secondary rotor provide considerable stiffening to the blade, the lower blade can be simplified to a semi-compliant representation with a single degree of freedom,  $\theta_{Bl}$ . The equation of motion is therefore reduced to

$$J'_{Bl}\ddot{\theta}_{Bl} = -J'_{Bl}\omega_{el}^2\Delta\theta_{Bl} - J'_{Bl}\gamma_{el}\Delta\dot{\theta}_{Bl} + M_{\theta l} - \{I_c + I_{Bl}\sin(\phi_{Bl})\}T_s. \quad (21)$$

With  $\phi_{Bl} = \psi_l$ .

### Hub Dynamics

The hub is considered as a rotating body with one degree of freedom. Its equation of motion is given by

$$J_H\ddot{\theta}_H = \sum_i Q_B^{[i]} - Q_c, \quad (22)$$

where  $Q_B$  represents the torque contribution of the  $i^{\text{th}}$  blade and  $Q_c$  represents the parasitic torque due to aerodynamic drag on the rotor cross arm. The torque contribution from each blade to the hub is given by the reaction force from the stiffness and damping terms in equations 17 and 21 such that

$$Q_{Bu} = \left\{ J_{Bu}\mathbf{R}(\beta) \begin{bmatrix} \omega_{eu}^2 & 0 \\ 0 & \omega_{fu}^2 \end{bmatrix} \mathbf{R}^{-1}(\beta) \begin{bmatrix} \Delta\theta_{Bu} \\ \Delta\phi_{Bu} \end{bmatrix} + J_{Bu}\mathbf{R}(\beta) \begin{bmatrix} \gamma_{eu} & 0 \\ 0 & \gamma_{fu} \end{bmatrix} \mathbf{R}^{-1}(\beta) \begin{bmatrix} \Delta\dot{\theta}_{Bu} \\ \dot{\phi}_{Bu} \end{bmatrix} \right\} \cdot \begin{bmatrix} 1 \\ 0 \end{bmatrix} \quad (23)$$

and

$$Q_{Bl} = J_{Bl}\omega_{el}^2\Delta\theta_{Bl} + J_{Bl}\gamma_{el}\Delta\dot{\theta}_{Bl}. \quad (24)$$

Equations 17, 21 and 22 describe the dynamics of the upper and lower blades and the rotor hub, fully describing the dynamics of the primary rotor given the appropriate structural constants and forcing terms. A description of how the aerodynamic forcing terms  $M_\theta$  and  $M_\phi$  are obtained is given in section 3.2.2 and a description of how the secondary rotor thrust force is obtained is given in section 3.3.

## 3.2.2 Primary Rotor Aerodynamics

### Overview of Primary rotor aerodynamics

The torque contribution from the upper and lower blades can be represented by the torque coefficient,  $C_Q$  such that

$$M_{\theta u} = \frac{1}{2}\rho A_U U_0^2 R_u C_{Qu}(\lambda, \theta, \beta) \quad (25)$$

$$M_{\theta l} = \frac{1}{2}\rho A_l U_0^2 R_l C_{Ql}(\lambda, \theta). \quad (26)$$

Here the torque coefficient is dependent on the angle of azimuth,  $\theta$ , the pitch angle,  $\beta$ , and the tip speed ratio,  $\lambda$ . With the tip-speed ratio given by

$$\lambda = \frac{\omega R}{U_0}. \quad (27)$$

Here, the rotational speed can either be considered to be uniform across the rotor with  $\omega = \dot{\theta}_H$ , or the local angular velocity of the blade can be used. Implicit in this representation is that the effects of Reynolds number are ignored over the considered operating range, as the torque coefficient is dependent on the non-dimensional parameter  $\lambda$ . This can be rationalised as the X-Rotor typically operates at very large Reynolds numbers  $\approx 10^7$  where by the aerodynamic behaviour is relatively stable with respect to changes in the Reynolds number.

Similarly, the radial flapwise moment can be characterised with it's own moment coefficient  $C_{\phi}$  such that

$$M_{\phi u} = \frac{1}{2} \rho A_U U_0^2 R_u C_{\phi u}(\lambda, \theta, \beta) \quad (28)$$

$$M_{\phi l} = \frac{1}{2} \rho A_l U_0^2 R_l C_{\phi l}(\lambda, \theta). \quad (29)$$

With these representations the aerodynamic forces on each primary rotor blade can be characterised by a pair of look up tables, 3D for the upper blades and 2D for the lower blades. The key task for the modelling of the primary rotor aerodynamics is therefore the accurate generation of these lookup tables using aerodynamic models.

The aerodynamic modelling of VAWTs is a less mature field than HAWT modelling, and a number of different modelling paradigms exist across a wide range of modelling fidelities including double multiple streamtube (DMS) models, actuator cylinder models, lifting line theory (LLT) models, panel models, actuator line models, and blade resolved CFD. In order to characterise the a sufficiently wide operational range for the primary rotor ( $-18 < \beta < 18$ ), ( $1 < \lambda < 6.5$ ) the rotor must simulated at 851 operating points. Because of this, computational speed was considered very important for the aerodynamic model, allowing new simulations to be completed quickly if changes are made to the primary rotor design. In this context; as DMS models are computationally fast, relatively simple to implement, and have previously been successfully validated against both experimental data and higher fidelity codes, it was decided that a DMS modelling tool based on the implementation in (Sharpe & Freris, 1990) would be developed to describe the aerodynamics of the primary rotor.

### DMS Overview

Applied for a 3D rotor, the DMS method involves a double discretisation of the rotor, first the rotor is discretised vertically into a number of rotor disks assumed to be aerodynamically independent, demonstrated in figure 4a. Each disk is then discretised into a number of strait edged streamtubes with the flow inside each streamtube characterised by the flow on the central streamline, as shown in figure 4b, each streamtube is allowed to expand to ensure that fluid moment is conserved. The interaction between the flow and the rotor is characterised by a tandem pair of actuator surfaces representing the flows interaction with the upwind and downwind rotor sections, as shown in figure 4c. In essence this reduced the problem to solving the 1 dimensional flow along each streamline to characterise each streamtube, and integrating over every streamtube to characterise the rotor behaviour.

The azimuthal location of the streamtubes are not know a priori, due to their dependence on the rotor loading distribution and the consequent streamtube expansion due to momentum conservation. To circumvent this issue, the rotor is discretised using the angle subtended between the rotor radius vector and the incident streamline, henceforth referred to as the blade angle  $\Theta$ , rather than the angle of azimuth  $\theta$ . Both  $\Theta$  and  $\theta$  are shown in figure 5a. Once the streamtubes are solved and the loading distribution is obtained, the angle of azimuth corresponding to a given blade angle can be obtained from integrating outward from the central streamline with

$$\theta_{[u]}(\Theta) = \pi + \int_{\pi}^{\Theta_{[u]}} \zeta_{[u]}(\tilde{\Theta}) d\tilde{\Theta}, \quad (30)$$

$$\theta_{[d]}(\Theta) = \int_0^{\Theta_{[d]}} \zeta_{[d]}(\tilde{\Theta}) d\tilde{\Theta}. \quad (31)$$

where the expansion coefficients are given by

$$\zeta_{[u]} = \left[ \frac{2(1 - 2a_{[u]})(1 - a_{[d]})}{(1 - 2a_{[u]})(1 - a_{[d]}) + (1 - a_{[u]})} \right], \quad (32)$$

$$\zeta_{[d]} = \left[ \frac{2(1 - a_{[u]})}{(1 - 2a_{[u]})(1 - a_{[d]}) + (1 - a_{[u]})} \right], \quad (33)$$

where  $a_{[u]}$  and  $a_{[d]}$  represent the upwind and downwind induction factors.

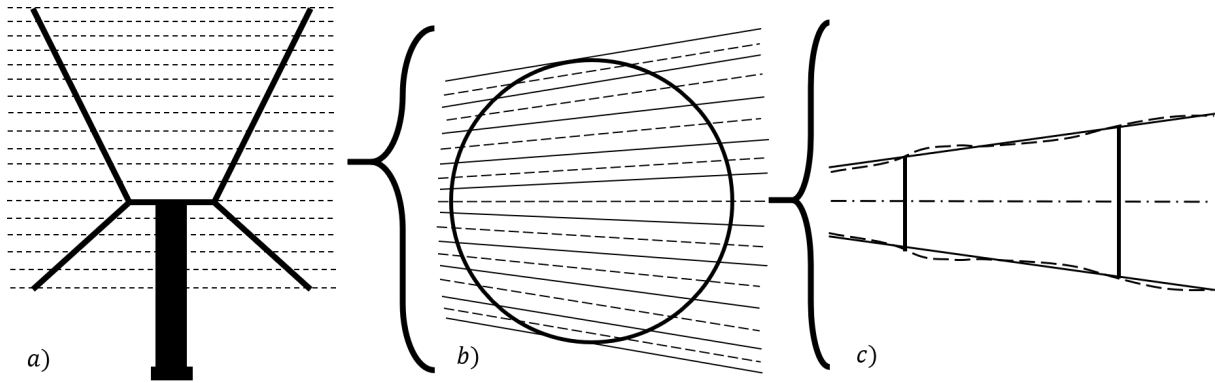


Figure 4: Discretisation procedure used for DMS simulations.

At each actuator surface, the flow is reduced to a one dimension problem where the retardation of the flow through an actuator surface is characterised by the induction factor,  $a$ , with

$$U_{I[u/d]} = (1 - a_{[u/d]})U_{N[u/d]} \quad (34)$$

where  $U_I$  represents the wind speed at the actuator surface,  $U_N$  represents the wind-speed at the actuator surface if the surface was not present and the subscripts  $[u/d]$  are introduced to specify if variables refer to the upwind or downwind actuator surfaces. At the upwind actuator surface,  $U_N$  is given by the free stream velocity  $U_0$ , whilst at the downwind actuator surface it is assumed that atmospheric pressure has been recovered thus the  $U_{N[d]}$  is given by

$$U_{N[d]} = (1 - 2a_{[u]})U_0. \quad (35)$$

At each actuator surface, the induction factors are calculated using blade element momentum theory; whereby the rotation averaged force from the blade element projected in the stream wise direction is balanced with the momentum change due to retardation of the flow. This is ensured by matching the thrust coefficient obtained from momentum theory

$$C_{TM[u/d]} = 4a_{[u/d]}(1 - a_{[u/d]}), \quad (36)$$

and the thrust coefficient obtained from the rotor averaged blade element forces

$$C_{TBE[u/d]} = \left[ \sec(\Theta) \frac{Nc}{2\pi r} \right] \left[ \frac{U_{a[u/d]}}{U_{N[u/d]}} \right]^2 \left[ C_n(\alpha_{[u/d]})\cos(\Theta)\cos(\psi) - C_t(\alpha_{[u/d]})\sin(\Theta) \right]. \quad (37)$$

The first term represents the rotation averaging, with  $N$  representing the number of blades,  $c$  representing the local chord length, and  $r$  representing the local radius. The second term is an artefact of the de-dimensionalisation and represents the ratio between apparent velocity at

the blade element,  $U_a$  and the incident velocity at the actuator surface in the no-load scenario. The final term represents the projection of the blade element force onto the streamline, with  $C_n$  and  $C_t$  representing the normal and tangential force coefficients,  $\alpha$  representing the angle of attack, and  $\psi$  representing the angle between the blade normal plane and the rotor plane. The lift, drag, normal and tangential axes, as well as the associated blade angles are shown figure 5b.

Both the apparent velocity and the angle of attack can be evaluated from figure 5, and are given by

$$U_{a[u/d]} = \sqrt{[\omega r + U_{I[u/d]} \cos(\Theta)]^2 + [U_{I[u/d]} \sin(\Theta) \cos(\psi)]^2}. \quad (38)$$

$$\alpha_{[u/d]} = \text{atan} \left( \frac{U_{I[u/d]} \sin(\Theta) \cos(\psi)}{\omega r + U_{I[u/d]} \cos(\Theta)} \right) + \beta. \quad (39)$$

Here it should be noted that, for simplicity, figure 5 represents the case where  $\psi = 0$ , however the general case is simply recovered by noting that the tangential component of velocity remains unchanged whilst the radial component of the velocity vector is scaled with  $\cos(\psi)$ .

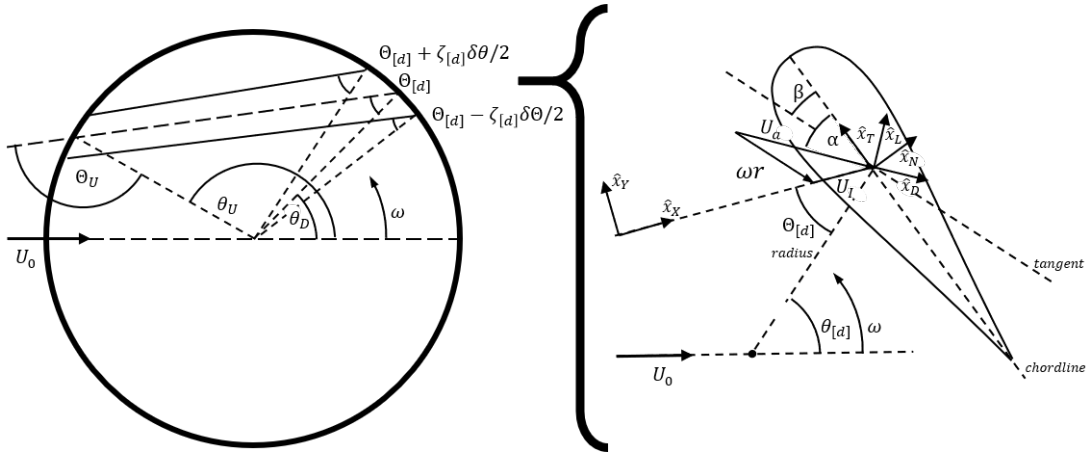


Figure 5: The streamtube and blade element geometries used in the DMS method

The blade torque can be obtained by numerically integrating the elemental torque contribution over the blade span

$$M_\theta(\theta) = \int_0^l \frac{1}{2} \rho U_I(\theta, s)^2 c D_Q(\theta, s) ds \quad (40)$$

where the local torque contribution is given by

$$D_Q(\theta) = r [C_n \sin(\beta) + C_t \cos(\beta)] \pm (0.25 - \xi) c [\{C_n \cos(\beta) - C_t \sin(\beta)\} \cos(\psi)]. \quad (41)$$

Here, the  $\pm$  sign refers to the upwind and downwind case respectively and  $\xi$  represents the relative attachment position of the aerofoil (measured from the leading edge). The radial flap-wise bending moment can similarly be evaluated by integrating the moment contribution over the rotor span

$$M_\phi(\theta) = \int_0^l \frac{1}{2} \rho U_I(\theta, s)^2 c D_R(\theta, s) ds, \quad (42)$$

with the local moment contribution given by

$$D_R(\theta) = s [C_n \cos(\beta) + C_t \sin(\beta)]. \quad (43)$$

Care must be taken in the evaluation of equations 40 and 42 to ensure that the integration is taken at a specific azimuth angle rather than at a blade angle as streamtube expansion is non-uniform over the rotor height.

There are a number of additional corrections that must be applied to the DMS model to describe the aerodynamic phenomena that are experienced by the rotor but not inherently modelled in the DMS algorithm. These include:

- Dynamic Stall,
- Streamline Curvature,
- Tip loss,
- Turbulent wake state.

The correction factors applied to account for these effects are given below.

### Dynamic Stall

Dynamic stall occurs when an aerofoils unsteady motion lead to the angle of attack exceeding the static stall angle. It is typically characterised by an increase in the lift coefficient beyond the maximum static value at angles of attack exceeding the static stall angle as flow separation is delayed, followed by a sharp increase in drag coefficient and drop in the lift coefficient as the flow separates. During reattachment, the lift coefficient remains below it's static value until the flow has reattached. A thorough discussion of the phenomena can be found in (Leishman, 2016).

To account for dynamic stall, the model of Masse (Masson, Leclerc, & Paraschivoiu, 1998) which interpolates between the dynamic force coefficients obtained from Strickland's modified Gormont dynamic stall model and the static blade polars is applied;

$$C_{[L/D]_{mod}} = \begin{cases} C_{[L/D]_{static}} + \left[ \frac{A_M \alpha_{ss} - \alpha}{A_M \alpha_{ss} - \alpha_{ss}} \right] (C_{[L/D]_{dyn}} - C_{[L/D]_{static}}) & \text{for } |\alpha| \leq |A_M \alpha_{ss}| \\ C_{[L/D]_{static}} & \text{for } |\alpha| > |A_M \alpha_{ss}| \end{cases}, \quad (44)$$

where  $C_{[L/D]}$  represents either the lift or drag coefficient, and  $A_M$  is an empirical constant, in this case given by 6. The dynamic lift and drag coefficients are calculated using Strickland's modification to the Gormont model and are given by

$$C_{L_{dyn}} = C_{L_{static}}(\alpha_{dyn}) \left( \frac{\alpha}{\alpha_{dyn} - \alpha_0} \right), \quad (45)$$

$$C_{D_{dyn}} = C_{D_{static}}(\alpha_{dyn}). \quad (46)$$

Where  $\alpha_0$  represents the zero lift angle of attack, and  $\alpha_{dyn}$  is given by

$$\alpha_{dyn} = \begin{cases} \alpha - \tau (|c \dot{\alpha} / [2U_a]|)^{0.5} & \text{for } |\dot{\alpha}| > 0 \\ \alpha + 0.5\tau (|c \dot{\alpha} / [2U_a]|)^{0.5} & \text{for } |\dot{\alpha}| \leq 0 \end{cases}, \quad (47)$$

with  $\tau$  given by

$$\tau = \begin{cases} 1.4 - 6(0.06 - t/c) & \text{for } C_L \\ 1.4 - 2.5(0.06 - t/c) & \text{for } C_D \end{cases}, \quad (48)$$

where  $t$  represents the aerofoil thickness. The time history used to calculate  $\dot{\alpha}$  is generated from the deterministic angle of attack calculated without induction factors.

The normal and tangential force coefficients used in equation 37 are recovered from the lift and drag coefficients using a simple coordinate transform

$$\begin{bmatrix} C_n \\ C_t \end{bmatrix} = \begin{bmatrix} \cos(\alpha) & \sin(\alpha) \\ \sin(\alpha) & -\cos(\alpha) \end{bmatrix} \begin{bmatrix} C_L \\ C_D \end{bmatrix}. \quad (49)$$

### Streamline Curvature

The effect of streamline curvature, also sometimes referred to as virtual incidence or virtual camber, describes the change in aerofoil behaviour between rectilinear and curvilinear flow. Typically, blade element polars are obtained from either wind tunnels or from simulation tools, both of which enforce rectilinear flow conditions. A blade section orbiting a central point sees curvilinear streamlines changing the local velocity and pressure distributions around the aerofoil and introducing a virtual camber and virtual incidence effects

To account for this effect, an angle of attack correction was derived for use in this tool exploiting the similarity between the orbital motion of the aerofoil and that of a pitching flat plate, the corrected angle of attack is then given by

$$\alpha' = \alpha + \cos(\psi) \left\{ \frac{1}{4} \frac{c}{r} + \frac{1}{2} \frac{(1 - 2\xi)c}{r} \right\}. \quad (50)$$

### Tip losses

To account for tip-losses, a modification of prandtl's tip loss function is applied. The tip loss function has the form

$$F = \frac{2}{\pi} a \cos \left( \exp \left[ -\pi \frac{(1-s)}{d} \right] \right), \quad (51)$$

Where  $d$  represents the spacing between the impermeable disks that approximate the complex wake structure. In this case sharpe's modification to the disk spacing was used (Sharpe & Freris, 1990) such that

$$d = U_{w[u/d]} \frac{\pi R}{NU_0}. \quad (52)$$

This is applied to the momentum theory calculations with the thrust coefficient modified such that

$$C_T = 4a(1-a)F. \quad (53)$$

### Turbulent wake state

To properly account for the transition to a turbulent wake state whilst the tip-loss correction is applied, the model uses the formulation proposed in (Buhl Jr, 2005) to modify the thrust coefficient calculation through extrapolation with a quadratic approximation, enforcing a smooth transition from  $a_T = 0.4$  to  $C_{TM}(1) = 2$ , such that the thrust coefficient is given by

$$C_{TM} = \begin{cases} \frac{8}{9} + (4F - \frac{40}{9})a + (\frac{50}{9} - 4F)a^2 & a \leq a_T \\ 2 & a > a_T \end{cases}. \quad (54)$$

### Validation

To ensure the accuracy of the proposed DMS model, it was validated against the higher fidelity lifting line code CACTUS (Murray & Barone, 2011). Lifting line codes inherently model the processes of both tip-loss and the transition to the turbulent wake state, and CACTUS includes a Leishman-Bedowes dynamic stall model (generally considered more accurate than the Gormont model), and a similar correction for streamline curvature to that which is applied in the DMS model.

Initially the CACTUS model was run without streamline curvature or dynamic stall corrections and is compared to the DMS model with corrections for tip losses and the turbulent wake state. The rotor power coefficients from each model are compared in figure 6 and the azimuthal variation in blade torque are compared in figure 7.

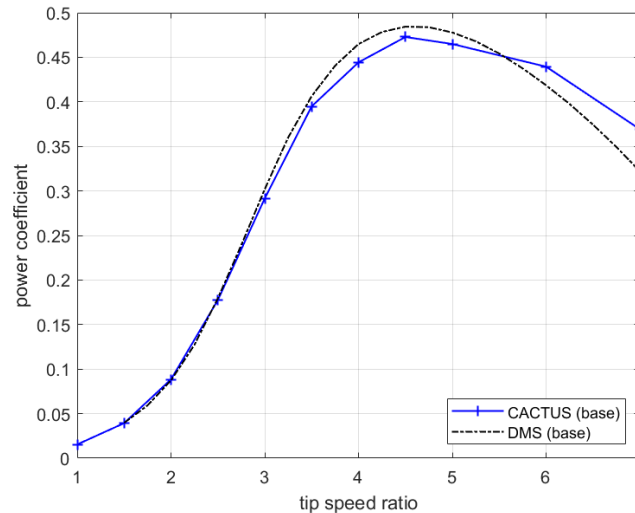


Figure 6: Comparison of the rotor power coefficient as simulated using the base DMS model and the Base LLT model

Figure 6 shows that there is a strong agreement between CACTUS and the DMS model over the range of tip-speed ratios considered. The agreement in the location and magnitude of the peak power coefficient is considerable, with both models predicting the peak power coefficient occurring at  $\lambda = 4.5$ , and the CACTUS and DMS model predicting the peak power coefficient to be 0.473 and 0.484 respectively, a difference of 2.3%. At high tip-speed ratios, the results begin to diverge. This is expected as momentum based models typically become less accurate at higher blockages, and the turbulent wake state correction factor is based on empirical relationships derived for a whole rotor disk, rather than a small actuator surface representing a portion of a rotor (as it is being applied in this case). In general though, the agreement between the DMS model and the higher fidelity code is considerable, and it can be inferred that the base DMS model provides an effective representation of rotor averaged behaviour.

Similarly, figure 7 shows very strong agreement in the azimuthal variation in torque coefficient predicted by both the CACTUS and the DMS models across the range of tip-speed ratios considered. The magnitude and location of the peak of the torque ripple is reproduced consistently across both models and the transition from a 4 peak torque ripple at low tip-speed ratios to a 2 peak torque ripple at higher tip-speed ratios is also well reproduced between both models. At high tip-speed ratios, the DMS model predicts a shallower trough in the torque ripple as the rotor transitions between the upwind and downwind rotor halves (at  $90^\circ$  &  $270^\circ$ ) however at  $\lambda = 6$  a lower power coefficient is still obtained as the DMS model consistently underestimates the torque coefficient aside from this. In general, the agreement between the DMS model and the higher fidelity code is considerable, and it can be inferred that the base DMS model provides an effective representation of azimuthal variations in rotor torque.

Following the successful validation of the base DMS model, the CACTUS model was re-run this time including both streamline curvature and dynamic stall corrections. This was then compared to the fully corrected DMS model. The rotor power coefficients from each model are compared in figure 8 and the azimuthal variation in blade torque are compared in figure

9.

Figure 8 shows that there is good agreement between fully corrected CACTUS and DMS models over the low to the intermediate range of the tip-speed ratios considered. The agreement in the location and magnitude of the peak power coefficient is reasonable, with the CACTUS and DMS models predicting the peak power coefficient occurring at a tip-speed ratio of 4.5 and 4.25 respectively, and predicting the peak power coefficient to be 0.474 and 0.458 respectively, a difference of 3.4%. At high tip-speed ratios, the results also diverge at a rate greater than the uncorrected models, this is most likely due to a difference in the formulation of the streamline curvature correction. The CACTUS documentation does not provide an exact formulation of the streamline curvature correction used in the code, so a thorough discussion of the differences cannot be provided. In general, the agreement between the DMS model and the higher fidelity code is considerable, and it can be inferred that the fully corrected DMS model provides an effective representation of rotor averaged behaviour at low and intermediate tip-speed ratios, but cannot effectively capture the behaviour at high tip-speed ratios. As the X-Rotor will not typically operate in this high tip-speed ratio range, the DMS model is considered to be sufficiently accurate representation of the rotor averaged behaviour for control modelling and control strategy evaluation.

Figure 9 shows very strong agreement in the azimuthal variation in torque coefficient predicted

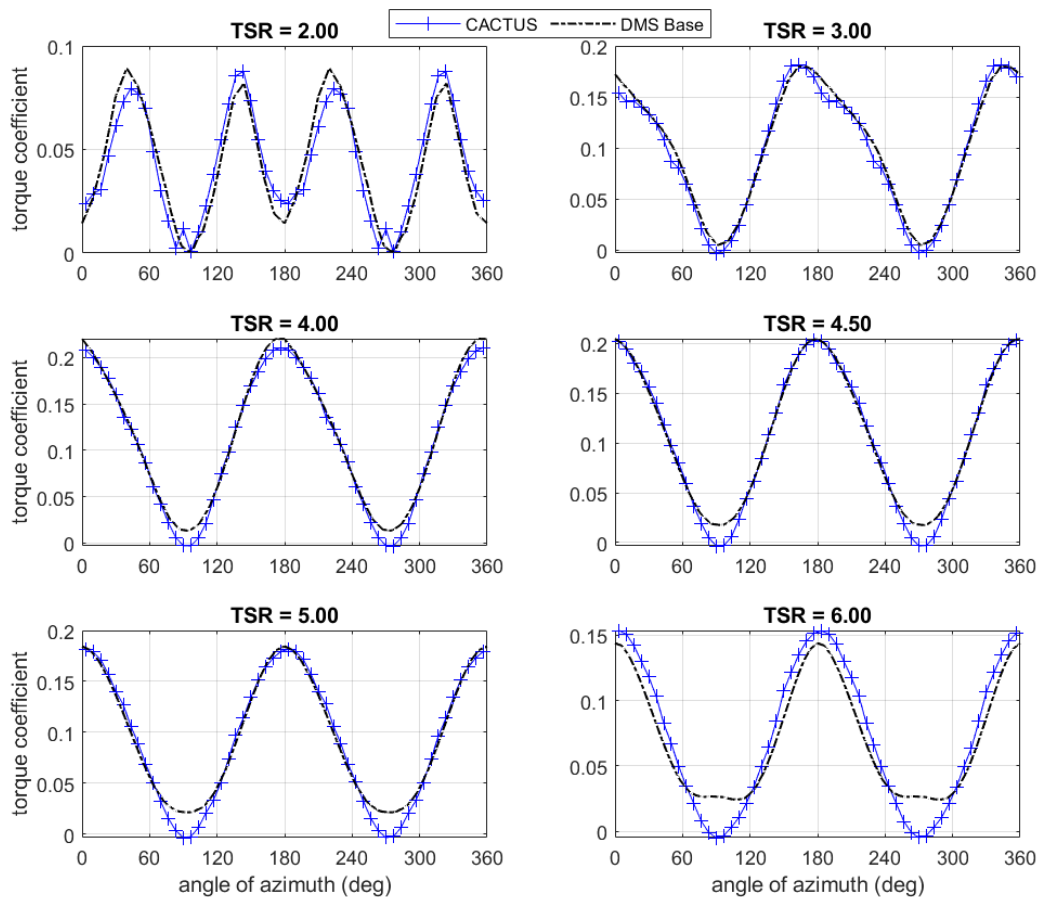


Figure 7: Comparison of the variation in torque coefficient as simulated using the base DMS model and the Base LLT model

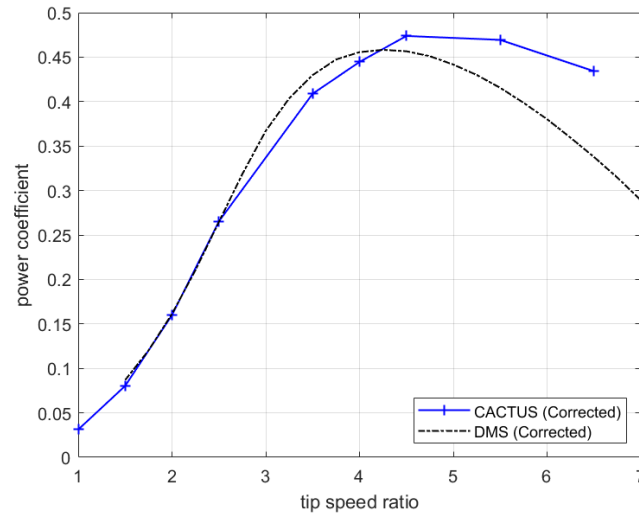


Figure 8: Comparison of the rotor power coefficient as simulated using the fully corrected DMS model and the fully corrected LLT model

by the fully corrected CACTUS and DMS models across the range of tip-speed ratios considered. The magnitude and location of the peak of the torque ripple is reproduced consistently across both models. At high tip-speed ratios, the DMS model predicts a shallower trough in the torque ripple as the rotor transitions between the upwind and downwind rotor halves (at  $90^\circ$  &  $270^\circ$ ) however at  $\lambda = 5.5$  a lower power coefficient is still obtained as the DMS model consistently underestimates the torque coefficient in the rest of the profile. In general, the agreement between the DMS model and the higher fidelity code is considerable, and it can be inferred that the fully corrected DMS model provides an effective representation of azimuthal variations in rotor torque, and can be used for control modelling purposes.

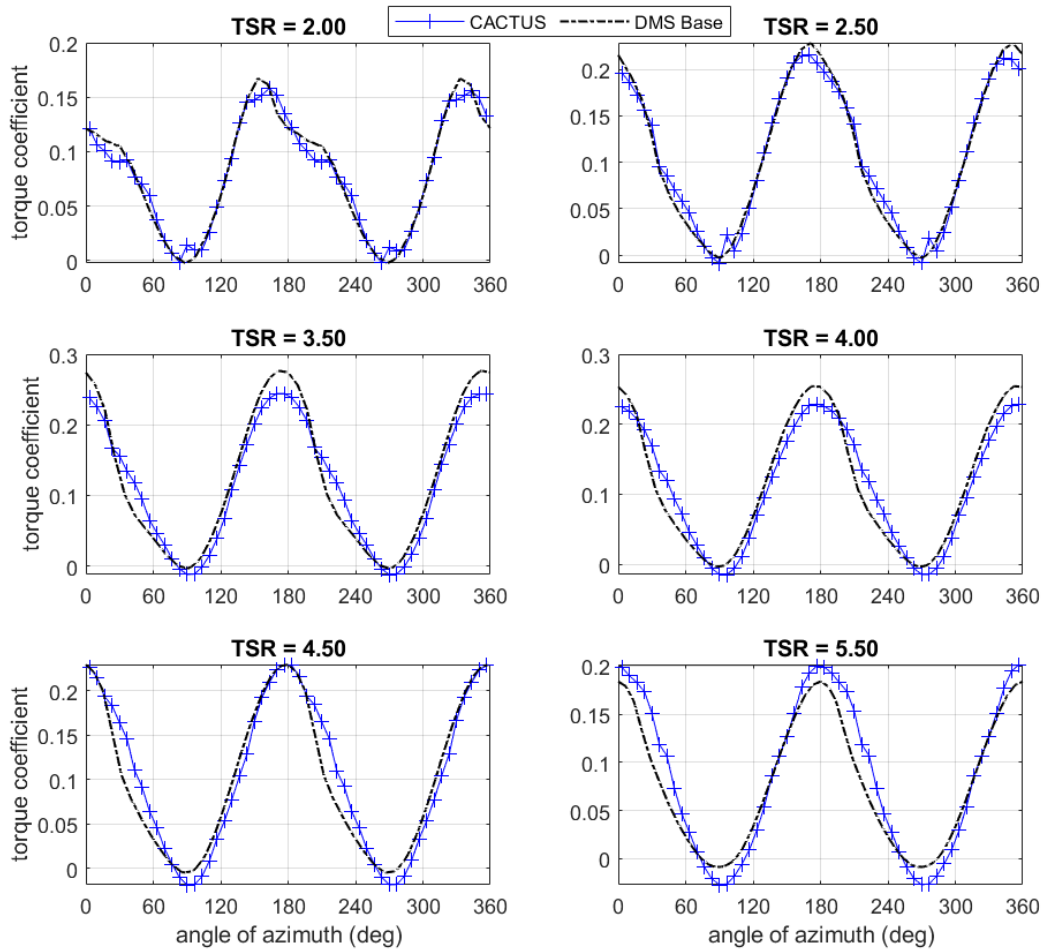


Figure 9: Comparison of the variation in torque coefficient as simulated using the fully corrected DMS model and the fully corrected LLT model

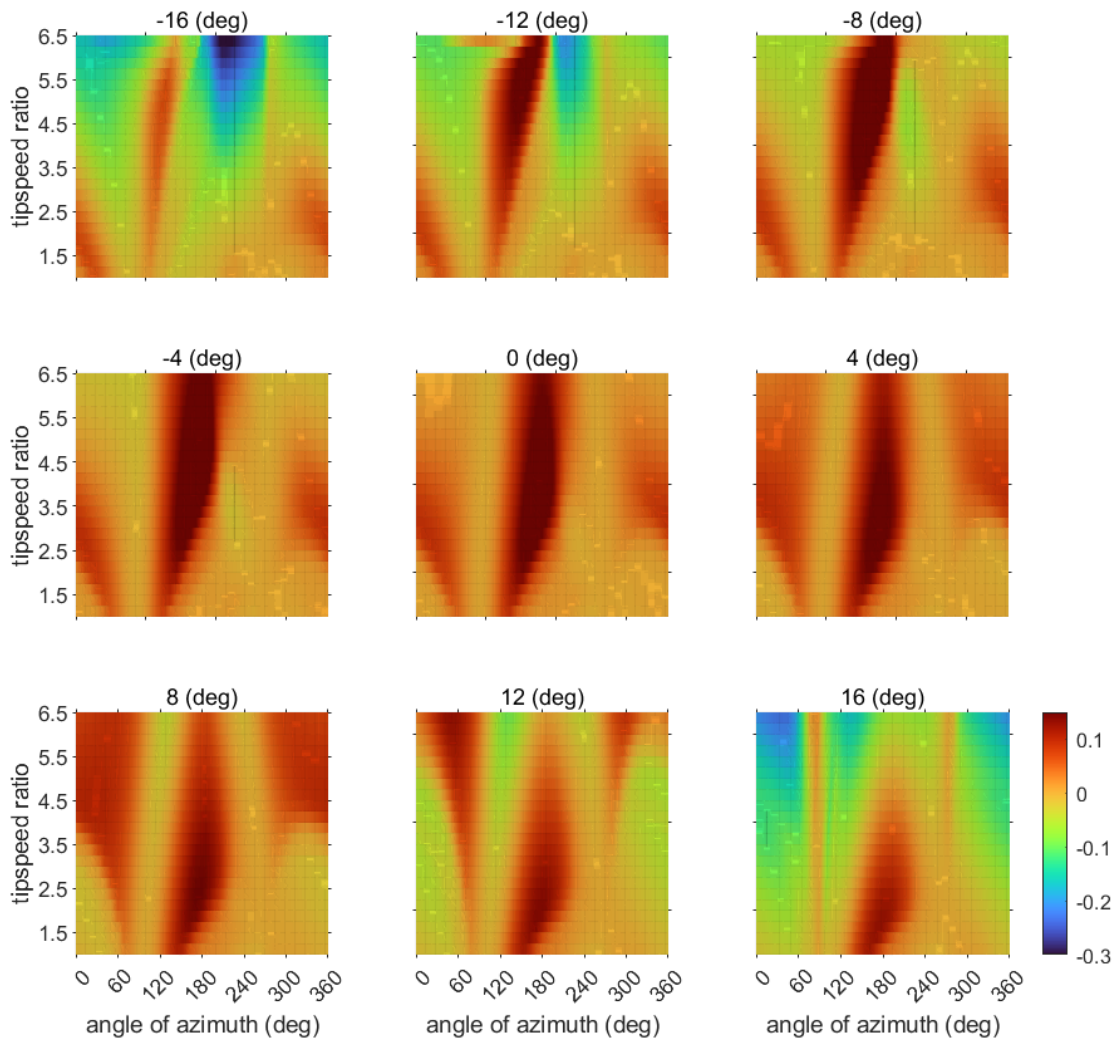


Figure 10: Upper blade torque coefficient  $M_\theta$  presented on the  $\lambda, \theta$  plane over a range of pitch offsets.

Using the DMS model, the variation in upper blade torque coefficient,  $M_\theta$ , and flapwise radial bending moment coefficient,  $M_\phi$ , was calculated over a range of fixed pitch offsets  $18^\circ \geq \beta \geq 18^\circ$  at intervals of  $1^\circ$ . The torque coefficient is presented on the  $\lambda, \theta$  plane for a number of pitch offsets in figure 10. The lower blade torque coefficient is shown on the  $\lambda, \theta$  plane in figure 11. The flapwise radial bending moment coefficient is presented on the  $\lambda, \theta$  plane for a number of pitch offsets in figure 12

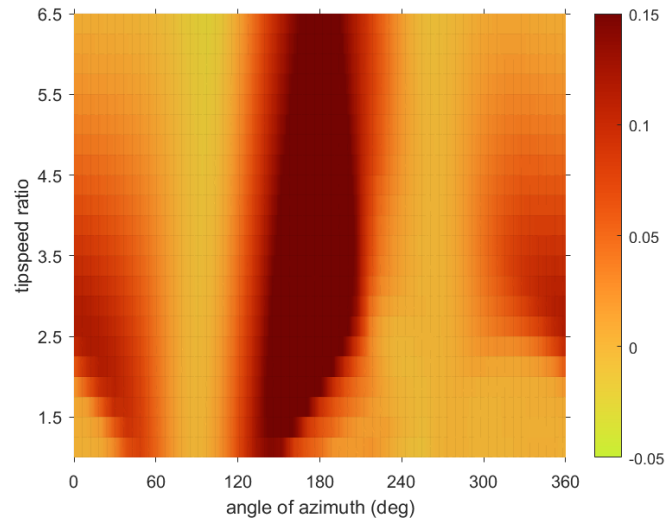


Figure 11: Lower blade torque coefficient  $M_\theta$  presented on the  $\lambda, \theta$  plane

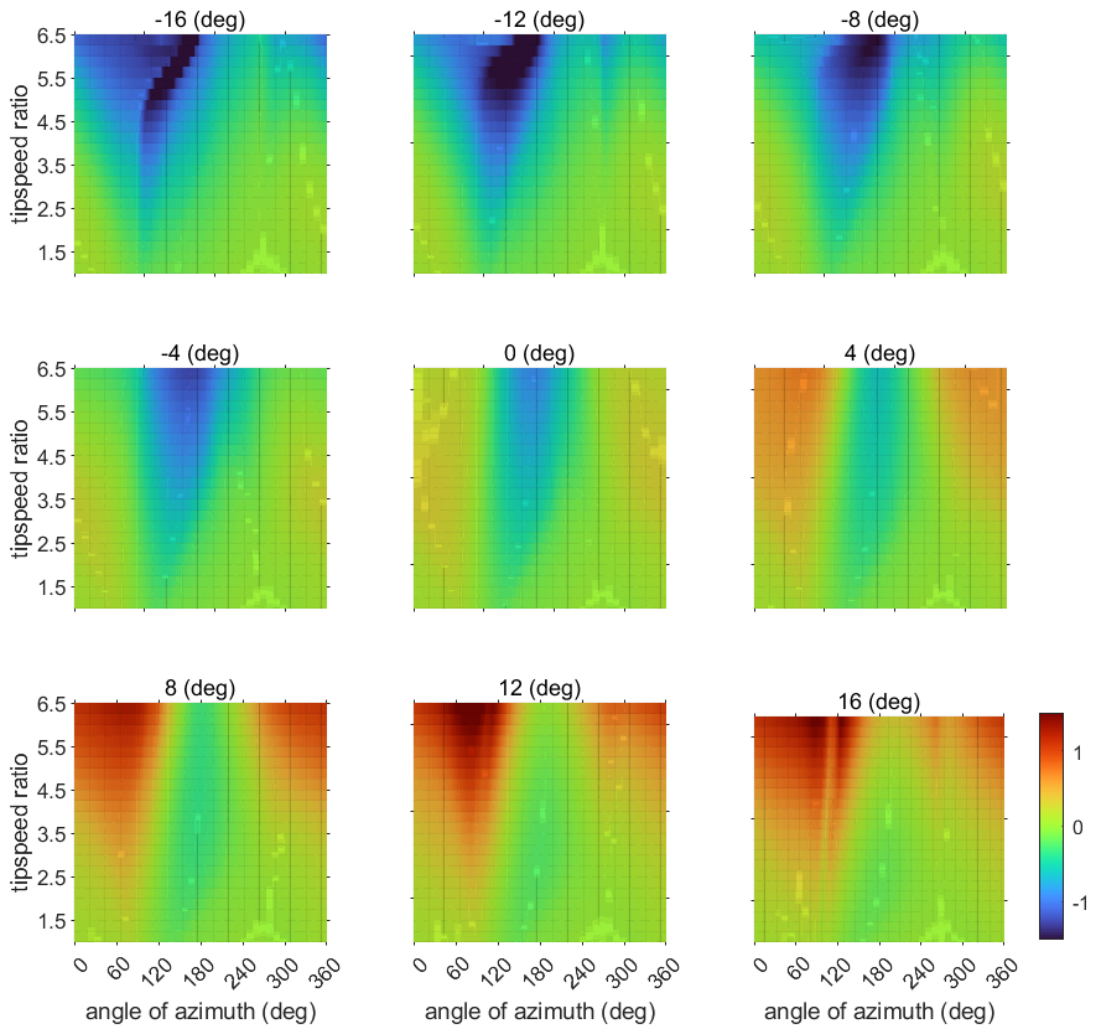


Figure 12: Upper blade radial flapwise moment coefficient  $M_\phi$  presented on the  $\lambda, \theta$  plane over a range of pitch offsets.

### Cross arm drag

The parasitic torque contribution from the crossarm rotor drag,  $Q_C$ , is calculated using the simplification that only the rotational component of velocity is considered. The torque contribution is given by

$$Q_C = N \int_0^{R_c} \frac{1}{2} \rho (\omega r)^2 c_c(r) C_{Dc}(r) r dr \quad (55)$$

Assuming that the crossarm has a constant chord and drag coefficient, the integral can be readily evaluated to obtain

$$Q_C = \frac{N}{8} \rho c_c C_{Dc} \omega^2 R_c^4. \quad (56)$$

### Aerodynamic damping

As the lower blades experience considerable damping from the secondary rotor thrust, aerodynamic damping will only be considered for the primary rotor. This can be modelled through approximating the detriment in wind speed experienced by the upper blade as it deforms. Such that the wind speed is given by

$$U_d = U_0 - U_{def} \quad (57)$$

where  $U_{def}$  is the relative velocity due to deformation at the aerodynamic centre of the blade,  $l_{Buca}$ .

Assuming the blade is rigid and hinges at the blade root. The relative motion of the blade in the windward direction is given by

$$U_{def} = l_{Buca} [\dot{\phi}_U \cos(\phi_U) \cos(\theta_U) + \dot{\theta}_U \sin(\theta_U)]. \quad (58)$$

This new corrected velocity  $U_d$  can be in the calculation of the aerodynamic loads  $M_\theta$  and  $M_\phi$ .

## 3.3 Power Take-Off Modelling

The power take-off has two components, the secondary rotors and the power-train. Note that additional information on the secondary rotor design can be found in Appendix A.

### 3.3.1 Secondary Rotor modelling

#### Secondary rotor dynamics

The secondary rotor is considered to be a rigid body rotating body, with the rotational speed governed by the equation

$$J_s \dot{\omega}_s = M_{\theta_s}(\lambda_s, U_s) - Q_{RG} \quad (59)$$

where  $J_s$  represents the secondary rotor inertia,  $\omega_s$  the secondary rotor rotational speed,  $M_{\theta_s}$  the aerodynamic torque on the secondary rotor,  $\lambda_s$  the secondary rotor tip-speed ratio,  $U_s$  the incident speed on the secondary rotor and  $Q_{RG}$  the shaft torque. The shaft torque is determined by the power train which is described in section 3.3.2, and the remainder of this sub-section will focus on the aerodynamic modelling of the secondary rotor to obtain the torque  $M_{\theta_s}$  and the thrust  $T_s$  on the secondary rotor.

#### Secondary rotor aerodynamics

The aerodynamic torque and thrust on the secondary rotors can be modelled using torque and thrust coefficients such that

$$M_{\theta_s} = \frac{1}{2} \rho A_s U_s^2 R_s C_{Q_s}(\lambda_s) \quad (60)$$

$$T_s = \frac{1}{2} \rho A_s U_s^2 C_{Ts}(\lambda_s) \quad (61)$$

Where the incident wind speed on the secondary rotor is given by the sum of the apparent wind speed due to the rotation of the primary rotor and the incident wind speed

$$U_s = \omega[l_c + l_{BI} \sin(\phi_{BI})] + U_0 \sin(\theta). \quad (62)$$

The torque and thrust coefficients for the secondary rotor can be obtained from BEM simulations. The design of the secondary rotors is detailed in appendix A. As the secondary rotors employ a five bladed design, they could not be simulated in either FAST or Bladed, as both programs have a maximum blade number of 3. Because of this, the BEM tool QBlade (Marten & Wendler, 2013) was employed to simulate the secondary rotors. Initially, to ensure that QBlade gave results comparable to FAST (Moriarty & Hansen, 2005), a representative 3 bladed rotor was modelled using both simulation tools, the thrust and torque coefficients are compared in figures 13.

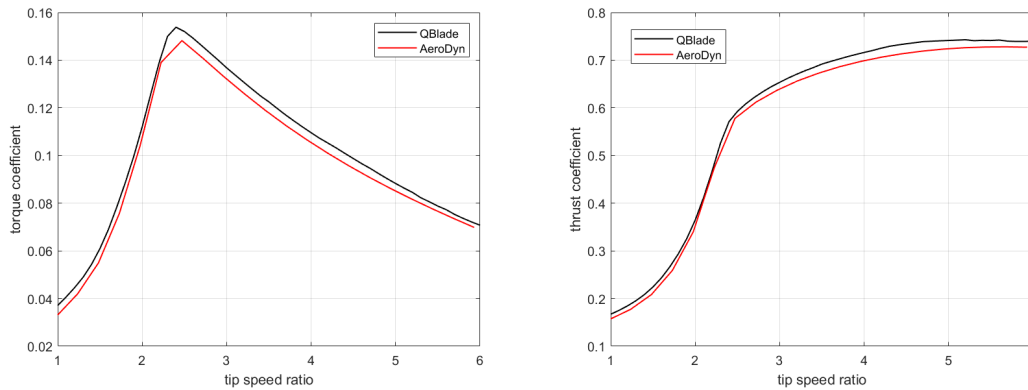


Figure 13: Torque and thrust coefficient comparison between QBlade and FAST(Aerodyn)

The agreement between the results from Qblade and the results from Aerodyn(FAST) are considered sufficient to allow the secondary rotor torque and thrust coefficients to be modelled in QBlade.

The current secondary rotor design includes a rotor hub with a radius that is 21% of the rotor radius, thus the modelling of the rotor hub is important if the aerodynamics of the secondary rotor are to be accurately represented. QBlade does not include hub modelling functionality but does include an optional blade root correction factor. To represent the effect of the hub, 3 assumptions were made about the hub design

1. The rotor hub has a thrust coefficient of 0.9
2. The rotor hub is designed such that blade root losses are minimised
3. The rotor hub is designed such that it has no effect on the aerodynamic torque

Assumption 1 allows the rotor thrust coefficient to be corrected for the hub with

$$C_{Ts} = C_{Tsaero} + 0.9 \left( \frac{R_{sh}}{R_s} \right)^2. \quad (63)$$

Assumption two informs the decision to disable blade root losses in the Qblade simulations, and assumption 3 indicates that the aerodynamic torque obtained from QBlade is representative of the total rotor torque. The final secondary rotor torque and thrust coefficient curves are shown in figure 14.

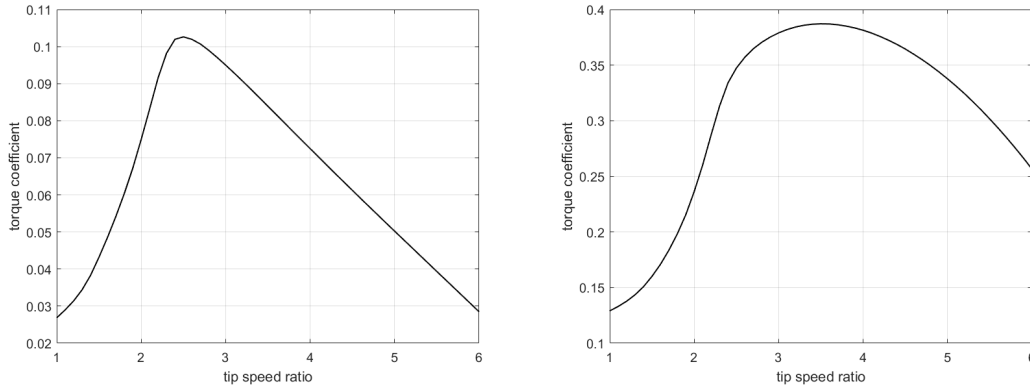


Figure 14: Torque and thrust coefficient for the secondary rotors

### 3.3.2 Power-train modelling

The secondary rotor power-train can be modelled with a compliant shaft connected to a direct drive generator. The dynamics of the compliant shaft is given by

$$\dot{Q}_{RG} = K_S(\omega_s - \omega_g) \quad (64)$$

where  $K_S$  represents the shaft stiffness and  $\omega_g$  represents the generator speed. The generator speed is then governed by

$$J_g \dot{\omega}_g = Q_{RG} - Q_M \quad (65)$$

where  $Q_M$  represents the mechanical torque from the generator. This mechanical torque is governed by the electrical dynamics of the generator with

$$Q_M = Q_e / \eta_g \quad (66)$$

where  $\eta_g$  represents the efficiency of the generator and  $Q_e$  represents the electrical torque. The electrical dynamics are governed by

$$\dot{Q}_e = k_e \left( \omega_g - \frac{\omega_e}{p} \right) \quad (67)$$

where  $\omega_e$  represents the electrical frequency,  $p$  represents the number of pole pairs in the generator and  $k_e$  represents the electrical stiffness. Assuming that the electrical dynamics are sufficiently high frequency, this representation can be simplified to allow the the mechanical torque from the generator to be directly controlled rather than modelled using equations 66 and 67.

The secondary rotor tip speed ratio can then easily be controlled using traditional torque control by ensuring

$$Q_M = k_c \omega_g^2 \quad (68)$$

with

$$k_c = \frac{1}{2} \rho A_s R_s^3 \frac{C'_{Q_s}}{\lambda_s'^2}. \quad (69)$$

The output power from the generator is then given by

$$P_g = T_M \omega_g \eta_g. \quad (70)$$

It is this approach that is currently employed in the control model.

## 4 Simulation Outputs

In this section a series of outputs using the control model are presented and interesting results are discussed. Note that the simulation results in the report are for an illustrative choice of parameters only. These will be updated using future outcomes from WP2, WP4 and WP5.

Simulation results are presented for a uniform wind speed in sub-section 4.2. These simulations show the general properties of the model and, whilst the parameter choices are illustrative, these simulations highlight the presence of rotational frequencies in each signal, as well as giving an illustrative idea of the potential magnitude of these oscillations (though to be clear, these magnitudes may differ significantly with different parameterisation). Details of the illustrative parameters used are discussed in sub-section 4.1.

In sub-section 4.3 simulation results are presented for a wind speed that ramps up in time. These simulations serve as a way of showing the illustrative variation in the key simulation outputs across a range of operating points.

Finally, in sub-section 4.5, illustrative simulation outputs are presented for a simulation using the effective wind speed model described in section 3.1.2. The wind speeds for each blade are presented and discussed.

### 4.1 Model Parameterisation

As discussed previously, where values are set for parameters throughout this report, they should be considered as an illustrative choice of parameters only. The parameters will be updated using future outcomes from WP2, WP3 and WP5. With that said, it is useful to describe how these illustrative parameters were set for transparency of the results.

Table 1 gives the variables associated with the primary rotor that have been given in (Leithead et al., 2019) and (Campos-Gaona, Stock, Morgan, Leithead, & Anaya-Lara, 2021).

Parameter	Value
$I_{Bu}$ (m)	100
$I_{Bl}$ (m)	65.3
$I_{ca}$ (m)	25
$\psi_u$ (deg)	30
$\psi_l$ (deg)	50
$A_U$ (m <sup>2</sup> )	8660
$A_L$ (m <sup>2</sup> )	4210
$m_{Bu}$ (kg)	40,500
$m_{Bl}$ (kg)	23,384
$m_s$ (kg)	10,000
$\omega_{eu}$ (rad s <sup>-1</sup> )	4.8381
$\omega_{fu}$ (rad s <sup>-1</sup> )	4.3354
$\omega_{el}$ (rad s <sup>-1</sup> )	3.2044
$\omega_{fl}$ (rad s <sup>-1</sup> )	3.7699
$J_g$ (kg m <sup>2</sup> )	1340
$p$	4

Table 1: Primary rotor variables given in previous reports

In order to populate the model, a number more variables are required that have not yet been rigorously derived/defined. In order to demonstrate the model capability, these variables must be populated with representative estimates, often based on rules that apply to 3 blades HAWTs and therefore may not be valid.

The total blade inertia can be estimated with

$$J_{Bt} = m_B l_{Bcm}^2 \quad (71)$$

and the effective blade inertia and effective contribution to hub inertia can be calculated using equation 15, and are given by

$$J_B h = \left(1 - \frac{B^2}{J_{Bt} C}\right) J_{Bt} \text{ and } J_B = \left(\frac{B^2}{J_{Bt} C}\right) J_{Bt}. \quad (72)$$

Taking initial representative estimates of  $B^2/(J_{Bt} C) \approx 2/3$ , and  $l_{Bcm} \approx 1/3$  allows the effective blade inertia and blade contribution to hub inertia to be readily calculated, these values are given in table 2. Treating the cross-arm as a uniform beam, the total cross arm inertia is given by

$$J_c = \frac{1}{12} \rho_{Lc} (2l_{ca})^3 \quad (73)$$

where  $\rho_{Lc}$  represents the mass per unit length of the cross arm. As the dimensions and material properties of the cross-arm are currently unavailable,  $\rho_{Lc}$  cannot be readily obtained. Here it is assumed that the mass per unit length will be similar to that of the mass per unit length of the blade root of the IEA 15MW reference wind turbine (Gaertner et al., 2020) ( $\rho_{Lc} \approx 3.1 \times 10^3 \text{ kg/m}$ ). The cross-arm inertia and the total effective hub inertia are given in table 2. The crossarm drag coefficient is assumed to be  $C_{Dc} = 0.05$  and the cross arm chord length is assumed to be 10m.

The damping constant of the blades can be approximated using an representative value of the damping ratio,  $\mu$  for composite blades with

$$\gamma_{[e/f]} = 2\mu\omega_{[e/f]}. \quad (74)$$

The damping constants for the upper and lower blades calculated typical value for the damping ratio of composite blades,  $\mu \approx 0.03$ , are given in table 2. Whilst the rotor shaft dimensions have not been defined, the rotor shaft can be assumed to very stiff with  $K_s \approx 10^7 \text{ Nm rad}^{-1}$ .

The variables associated with the secondary rotor are derived from the aerodynamic data presented in figure 14 and the secondary rotor design information presented appendix A. The necessary simulation parameters are given in table 3.

## 4.2 Control model outputs with uniform wind speed.

Initially, it is interesting to consider the system response to a uniform wind speed. Figures 15, 16 and 17 show the simulated power tracking, loading, and structural response of the X-Rotor with the simulation run at the X-Rotor's nominal rated speed of 12.5m/s.

From Figure 15 it is clear that the primary rotor tip speed ratio is well controlled by the secondary rotors, however the mean tip speed ratio is consistently lower than the design value ( $\lambda = 4.75$ ). This is likely due to the effect of aerodynamic damping reducing the predicted power coefficient of the rotor, as large radial flapwise deformations occurring around  $\theta = \pi$  lower the effective wind speed around the peak of the torque ripple, this is further explored in subsection 4.4.

Parameter	Value
$c_c$ (m)	10
$C_{Dc}$	0.05
$J_{Bu}$ (kg m <sup>2</sup> )	$3.00 \cdot 10^7$
$J_{Hbu}$ (kg m <sup>2</sup> )	$1.50 \cdot 10^7$
$J_{Bl}$ (kg m <sup>2</sup> )	$3.71 \cdot 10^7$
$J_{Hbl}$ (kg m <sup>2</sup> )	$1.86 \cdot 10^7$
$J_c$ (kg m <sup>2</sup> )	$3.23 \cdot 10^7$
$J_H$ (kg m <sup>2</sup> )	$9.94 \cdot 10^7$
$\gamma_{eu}$ (Nms rad <sup>-1</sup> )	0.26
$\gamma_{fu}$ (Nms rad <sup>-1</sup> )	0.23
$\gamma_{el}$ (Nms rad <sup>-1</sup> )	0.29
$\gamma_{fl}$ (Nms rad <sup>-1</sup> )	0.19
$K_s$ (Nm rad <sup>-1</sup> )	$10^7$

Table 2: X-Rotor simulation variables derived using representative assumptions.

Parameter	Value
$R_s$ (m)	4.7
$A_s$ (m <sup>2</sup> )	69.4
$k_c$ (N m s <sup>2</sup> rad <sup>-2</sup> )	38.82
$J_s$ (kg m <sup>2</sup> )	500

Table 3: Secondary rotor parameters for control model.

The primary rotor speed, and hence the primary rotor tip speed ratio has a strong 2P oscillation as the dynamics are dominated by the summed blade torques which are 1P dominated and are in anti-phase.

The secondary rotors also track the designed tip speed ratio successfully (within  $\pm 9\%$ ). The fluctuations in secondary rotor tip-speed ratio are dominated by the effect of the incident wind speed which occurs at 1P, although the fluctuations in the primary rotor speed provide a 2P component.

The total rotor power output oscillates at  $\pm 10\%$  around its mean value of 5.1MW. The oscillations are dominated by the 2P component arising from summing the two anti-phase 1P dominated secondary rotor power outputs.

From figure 16 it is clear that the aerodynamic torque on both the lower and upper blades is 1P dominated, with a large peak as the blade passes through  $\theta \approx 180$ , there is also a 2P component due to the torque peak in the back rotor half. The non-uniform loading trace also indicates that there will be significant higher order harmonic content.

As the counter torque provided by the secondary rotor thrust is larger than the aerodynamic torque on the lower blade, the net torque exchanged between the lower blade and the hub is negative. The secondary rotor loading is dominated by the effect of the incident wind speed and exhibits a strong 1P component. As expected, this leads the 1P component of the blade torques by a phase of approximately  $\pi/2$  as the peak wind speed experienced by the secondary rotor occurs at  $\theta = 90$ , whilst the peak blade torque occurs at approximately  $\theta = 180$ .

The net torque on the hub oscillates around zero (as the rotor is in steady state), and is dominated by a 2P component arising from summing the two anti-phase 1P dominated torques from each of the upper and lower blades. The radial flapwise root bending moment for the upper

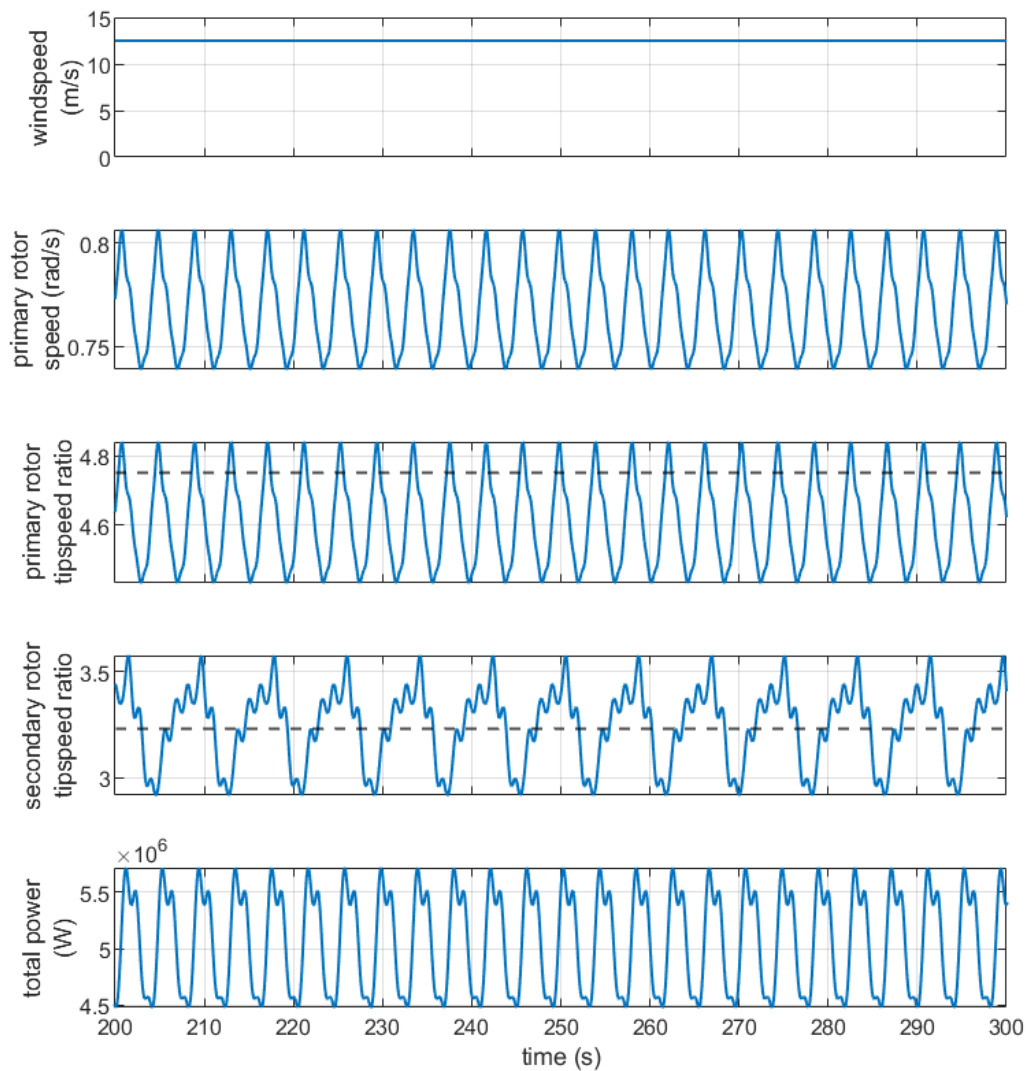


Figure 15: X-Rotor power tracking in a uniform wind speed of 12.5m/s.

blade oscillates at 1P with an amplitude of approximately 30kNm.

Figure 17 shows the structural response of the X-Rotor at uniform wind speed of 12.5m/s. As the net torque exchange between the upper blade and the hub is positive, the upper blade azimuth angle leads the hub azimuth angle. By a similar logic the lower blade lags the hub azimuth angle. Whilst the loading is dominated by 1P and 2P torque signals as shown in figure 16, higher order oscillatory components arising from the first edgewise frequency of both the upper and lower blades are clearly visible in both the upper and lower blades.

The offset in the upper blade vertical angle compared it's attachment angle are shown. These variations are approximately an order of magnitude larger than the variations in azimuthal deflection and lead to tip deflections oscillations of approximately  $\pm 7m$ . The edgewise blade frequency appears to be lightly damped, however the oscillations are of an amplitude of approximately  $0.5^\circ$  and  $1.5^\circ$  for the upper and lower blades respectively which are considerably

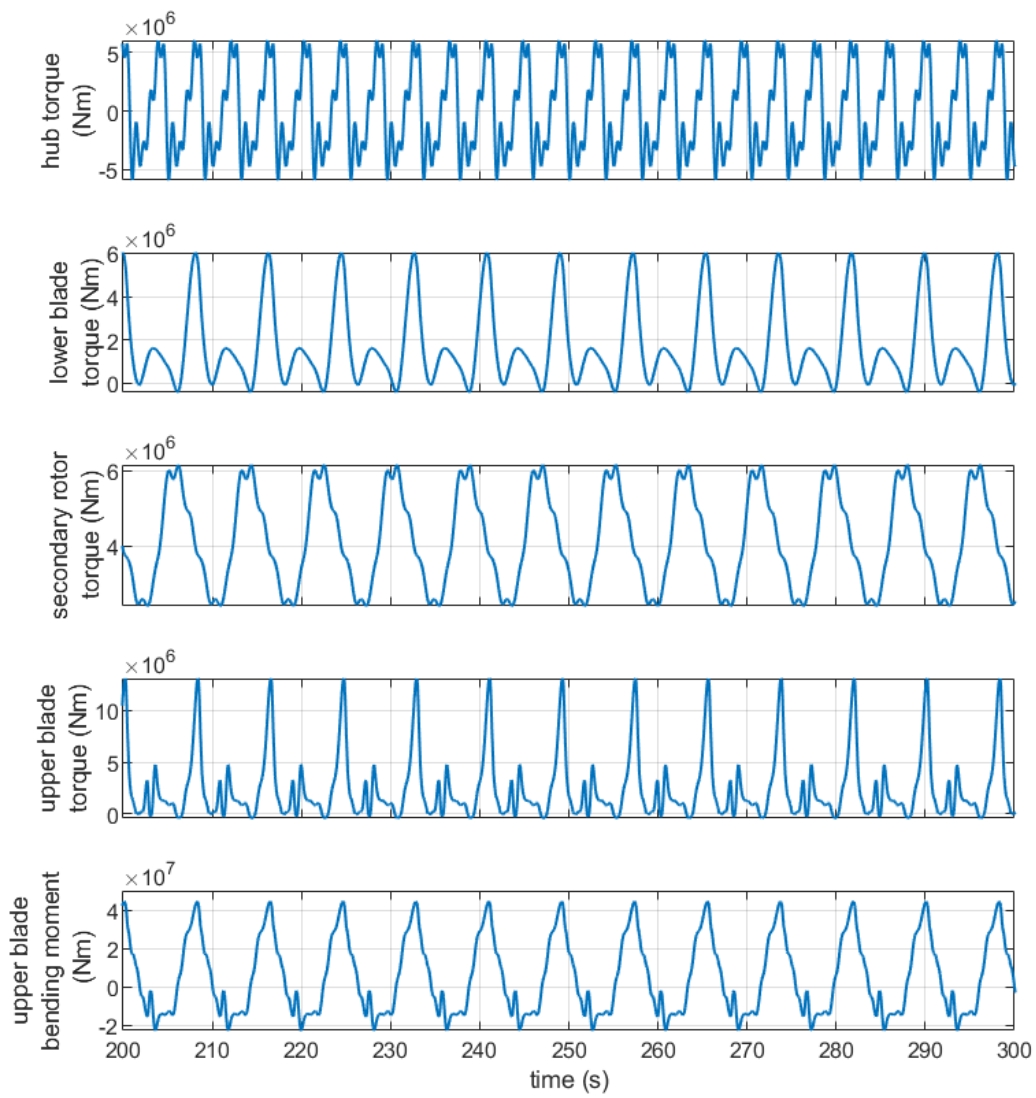


Figure 16: X-Rotor loads in a uniform wind speed of 12.5m/s.

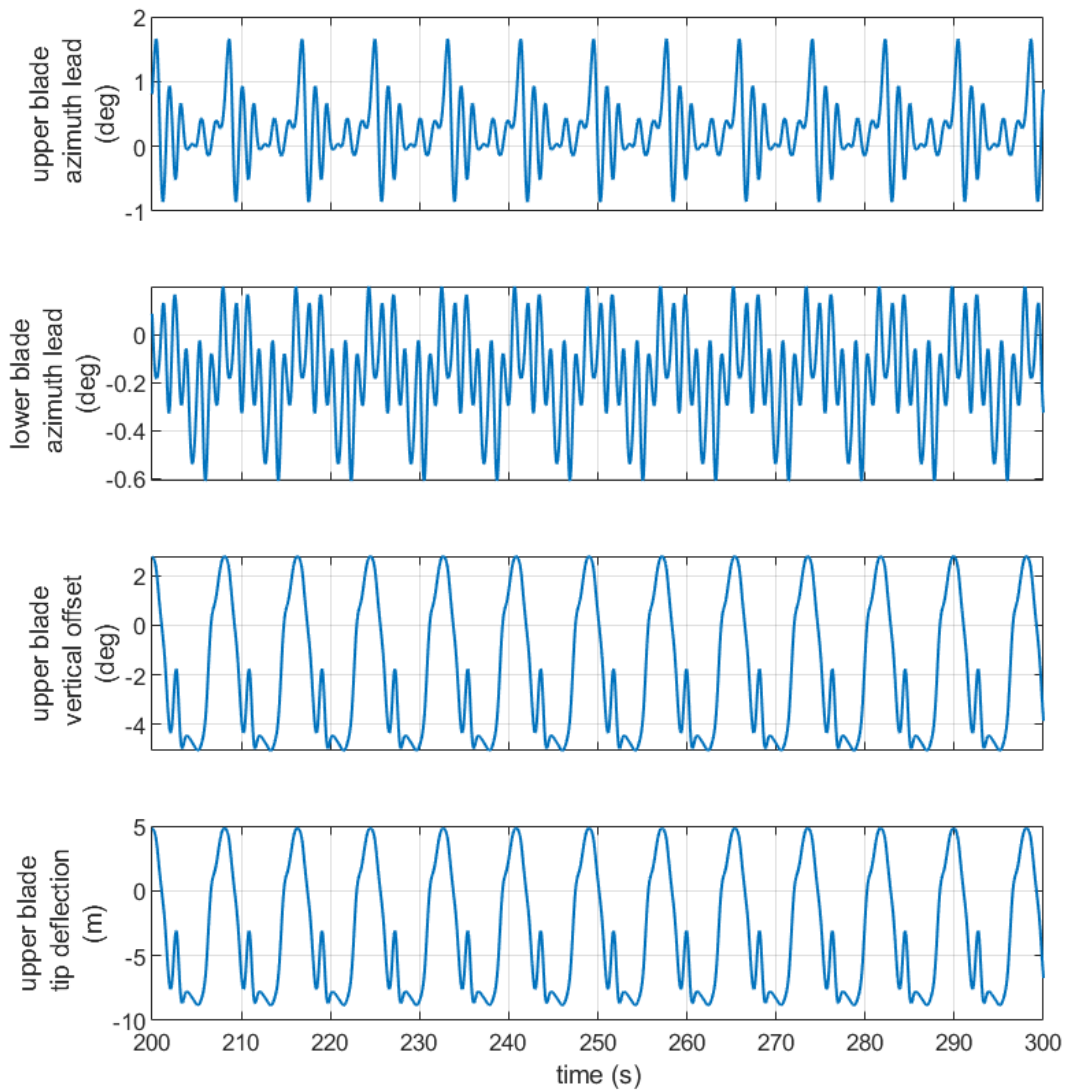


Figure 17: X-Rotor structural deflections in a uniform wind speed of 12.5m/s.

smaller than the flap wise deformations. The largest contribution to blade flap-wise bending is centrifugal force. Just as for HAWTs, the X-Rotor blades will be pre-bent so that they would attain the nominal shape in about 10m/s. To include this in the simulation, the deflection due to centrifugal force at 10m/s has been subtracted from the total blade deflection.

### 4.3 Control model outputs with wind speed ramp

Figures 18, 19 and 20 show the power tracking, loading and structural response of the X-Rotor to a steady wind speed slope from 3m/s 12.5m/s with a slope of 0.01 representing the below rated operating range of the X-Rotor.

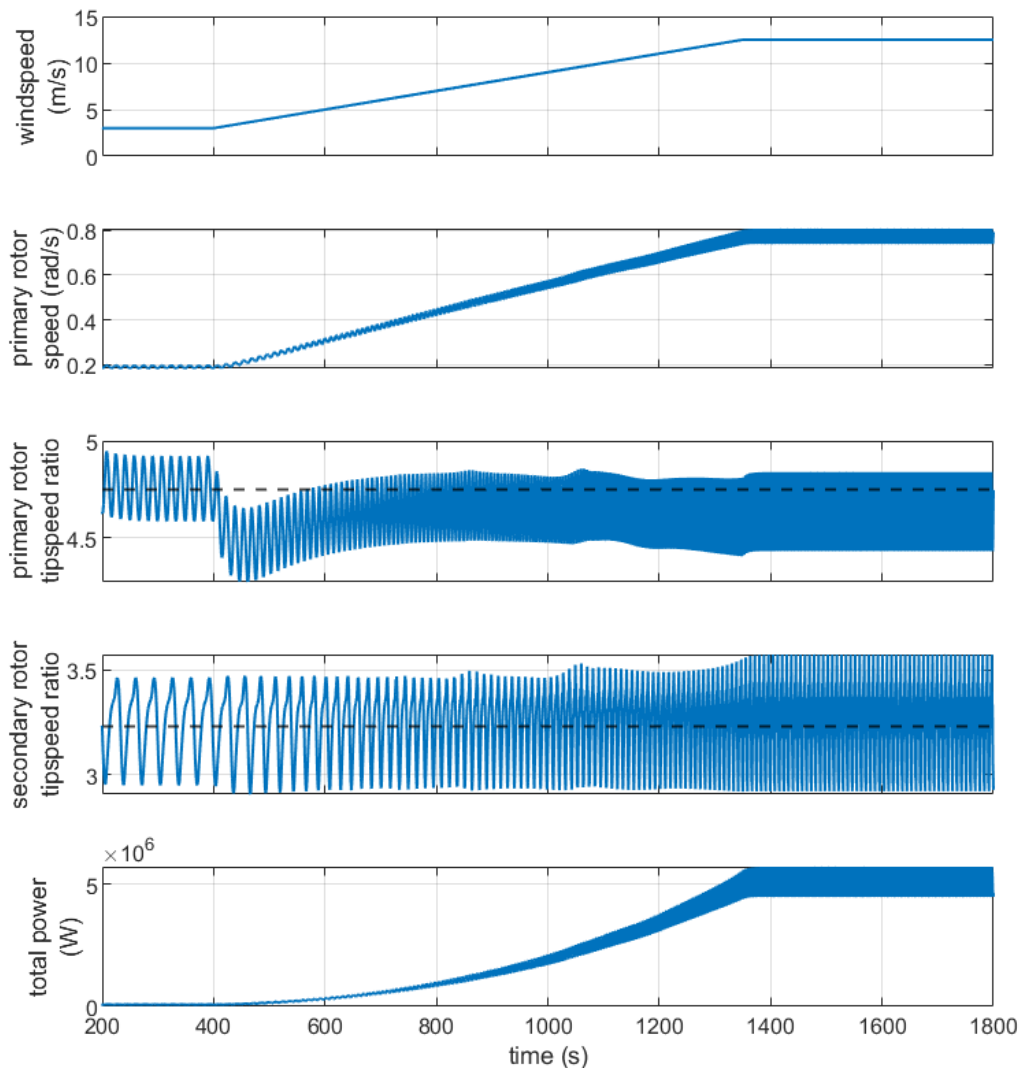


Figure 18: X-Rotor power tracking response to a steady change in wind speed from 3m/s to 12.5m/s

The ability of the secondary rotors to passively ensure primary rotor power tracking is evident, with the rotational speed of the rotor sufficiently controlled to maintain the primary rotor tip speed ratio. However, similarly to the case of a steady uniform wind speed, the primary rotor tip-speed ratio is consistently operating below its design value. This is investigated further in section 4.4

The rotor loading is shown in figure 19, and the structural response is shown in figure 20. There is no overshoot in the rotor loads or deflections compared to the uniform rated wind speed case.

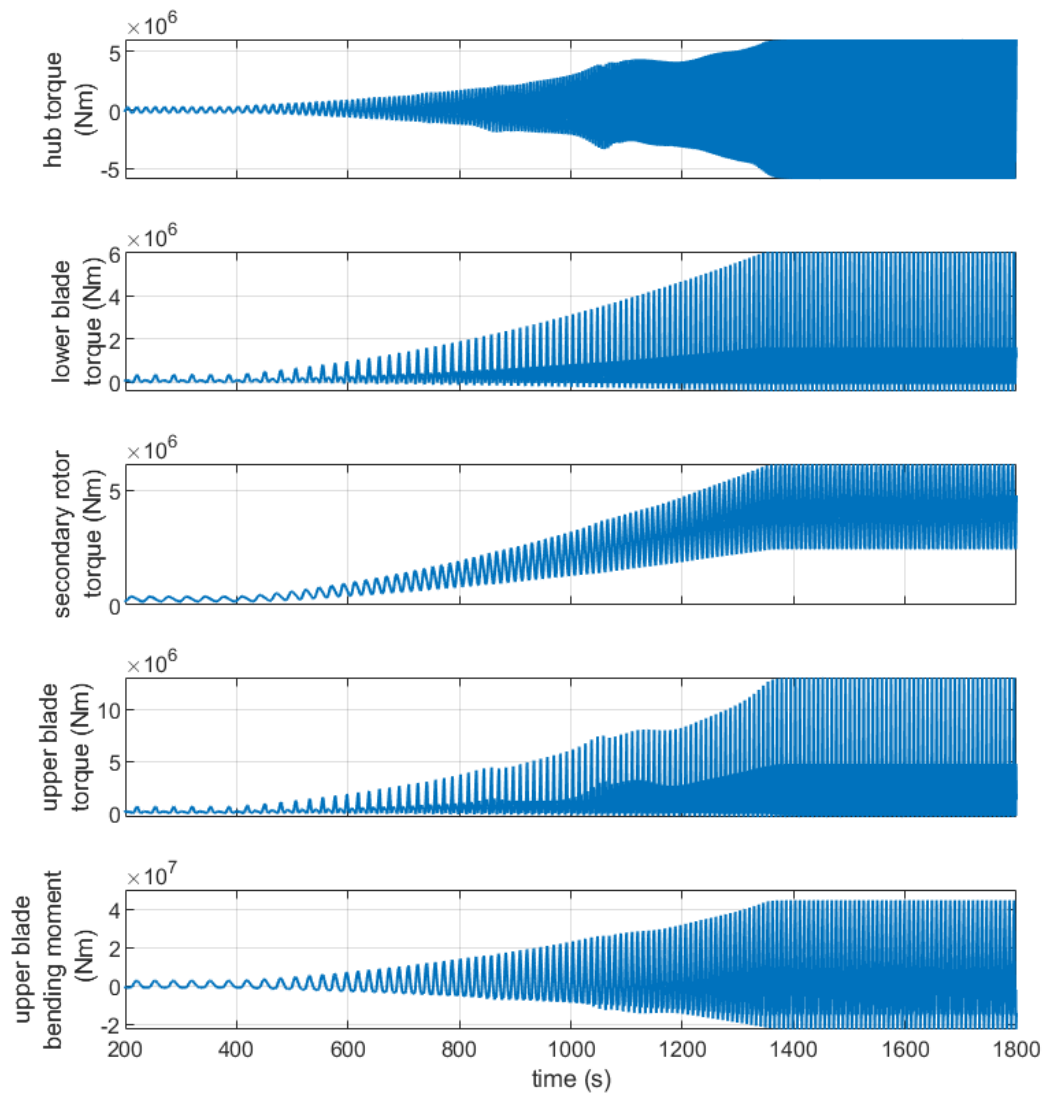


Figure 19: X-Rotor loading in response to a steady change in wind speed from 3m/s to 12.5m/s

As in the previous case, the deflection due to centrifugal force at 10m/s has been subtracted from the total blade deflection to account for the pre-bending of the blade.

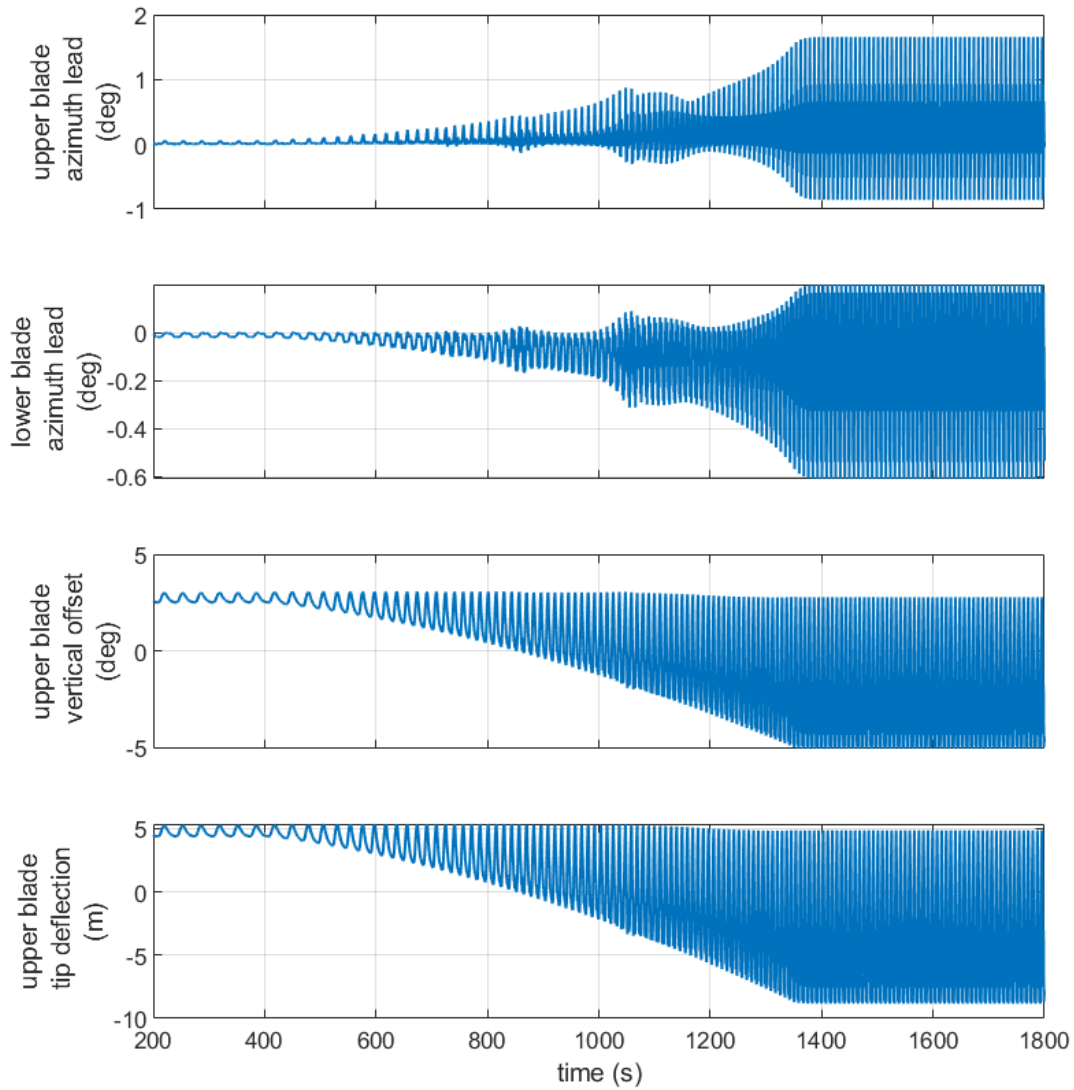


Figure 20: X-Rotor structural deflections in response to a steady change in wind speed from 3m/s to 12.5m/s

## 4.4 Effective of aerodynamic damping on primary rotor power tracking

Figure 21 shows the impact of modelling the effect of aerodynamic damping due to the motion of the upper blade on the power capture and tip speed ratio for a gradual uniform windspeed ramp up to rated. In this trace the wind is increased at a rate of  $0.002\text{m/s}^2$  from a windspeed of 3 m/s to the rated windspeed of 12.5m/s. The black line represents the simulation without the effect of aerodynamic damping and the red line represents the full simulation.

Comparing the red and black trace, it is clear that the inclusion of aerodynamic damping negatively impacts primary rotor power capture, and due to the fact that the primary rotor speed control is passively controlled by the design thrust coefficient of the secondary rotors this effects the operational point of the primary rotor. For the black trace, where aerodynamic damping is not modelled, the rotor behaviour is identical to the data that was used for the secondary rotor design, so the mean tip speed ratio is consistent with the design tip speed ratio.

Phenomenologically, the negative effect of aerodynamic damping on the power capture of the secondary rotor can be understood through considering that the velocity deficit that occurs due to the blade deformation is largest at the peak of the bending moment on the primary rotor. From figures 10 and 12, it can be seen that the peaks in flapwise bending moments occur at similar azimuthal locations to the peaks in primary rotor torque, negatively effecting power capture.

It is evident from figure 21 that as the windspeed increases, the difference between the design tip-speed ratio and the mean operational tip-speed ratio increases, this is because of the larger blade deflections at higher wind speeds having an increasing impact on rotor performance.

It should also be noted that a 5400s simulation was required to generate figure 21, and that on a commercial laptop the simulation was completed in around 30s clock-time, demonstrating the speed of the control model. It should also be noted that, with a properly design controller in the power take off model, the fluctuations in primary rotor speed, primary rotor tip-speed ratio, and primary rotor power should be damped to a much greater degree, and that the results here are to qualitatively demonstrate the effect of the inclusion of aerodynamic damping on the primary rotor power tracking, rather than to demonstrate a quantitative estimate of wind turbine performance.

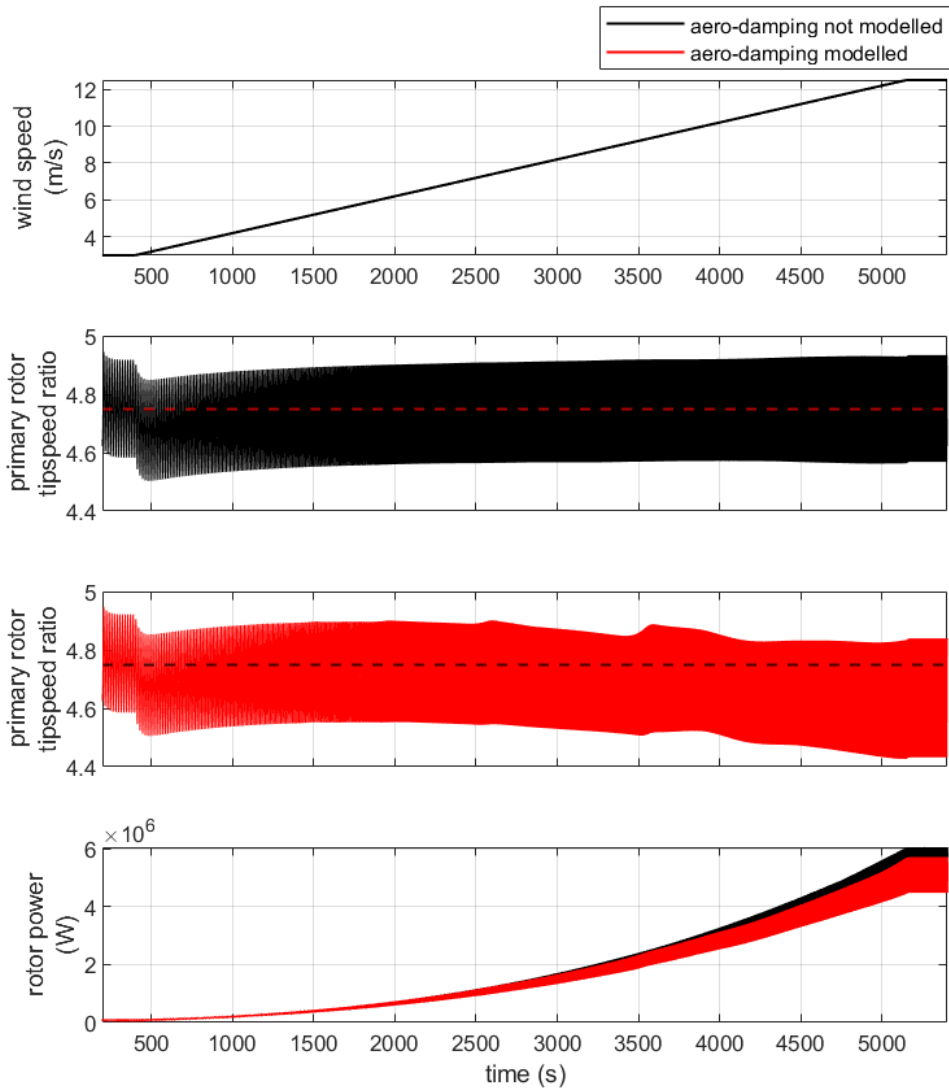


Figure 21: Caption

## 4.5 Model outputs with effective wind speed model

The effective wind speed model has been applied at a mean wind speed of 12.5 m/s. The rotor behaviour in terms of power tracking, loads, and structural response are shown in figures 22, 23, and 24 respectively.

As there is no pitch controller, the output power from the turbine is not limited as the wind speed exceeds the rated wind speed leading to excursions above the rated power. As in the previous power traces, the output power shows strong 2P oscillations due to the summation of the 1P dominated secondary rotor powers that are in anti-phase.

The upper blade tip deflections oscillate with an amplitude of approximately 9m, driven by the 1P oscillations in the bending moment and the oscillations in the azimuthal lead angle are limited to  $2^\circ$  and  $0.5^\circ$  degrees for the upper and lower blades respectively. It should, again, be emphasised that these values are generated from a model populated with estimated parameters, with many derived from rules of thumb that are applicable to HAWTs and may not be applicable to VAWTs. These results are presented as a qualitative demonstration of the simulation tool functionality, rather than a quantitative investigation into the expected rotor behaviour.

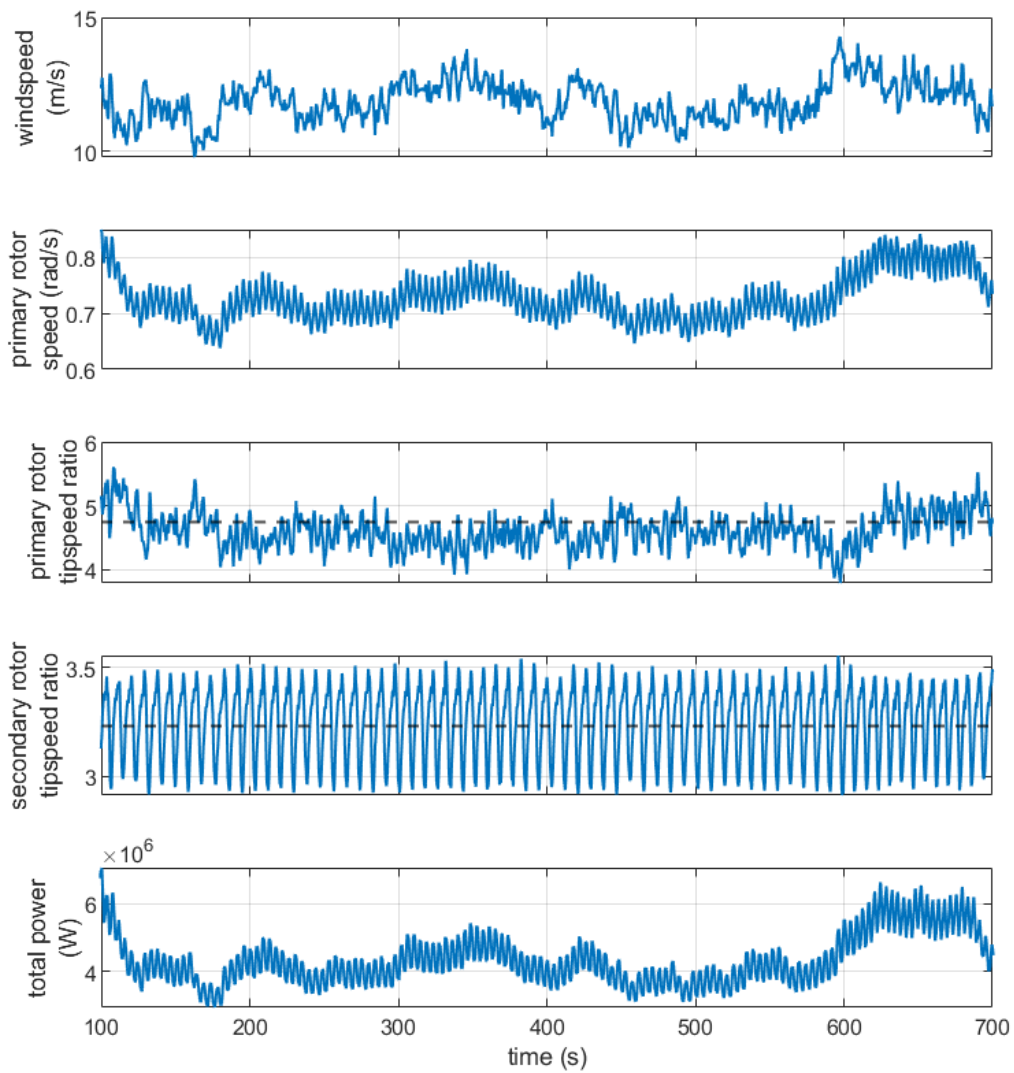


Figure 22: Power tracking response for the X-Rotor simulated with an effective wind speed model with a mean wind speed of 12.5m/s

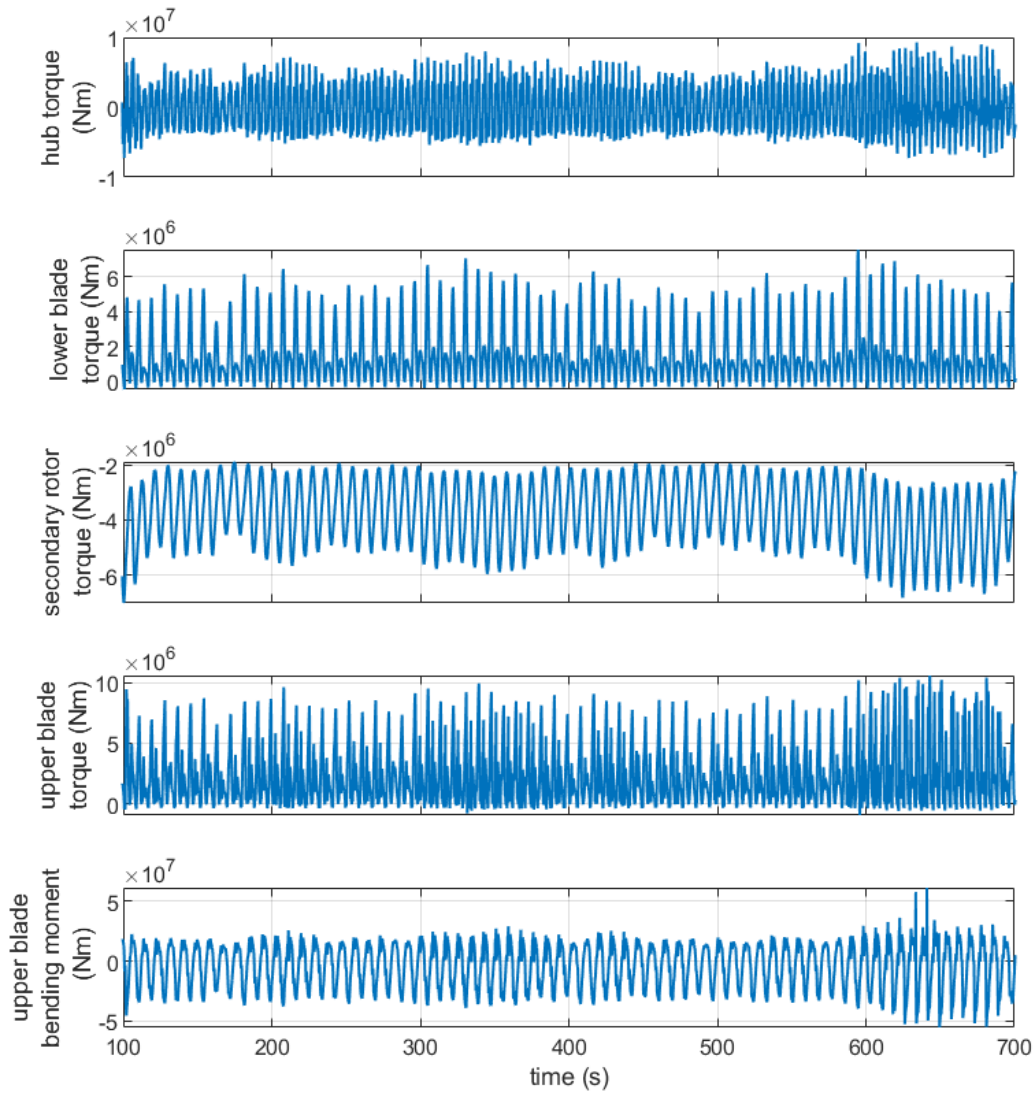


Figure 23: X-Rotor loads simulated with an effective wind speed model with a mean wind speed of 12.5m/s

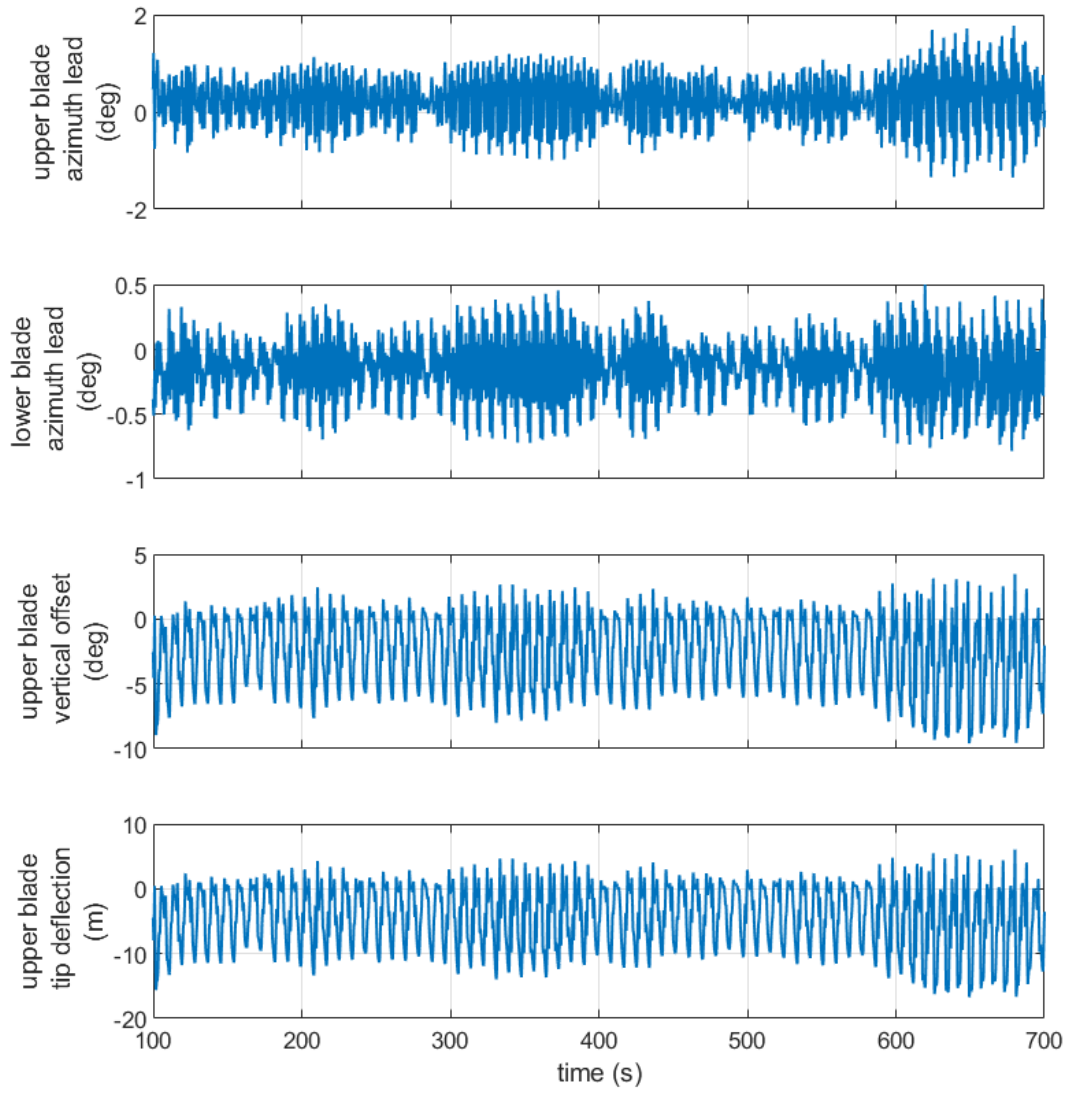


Figure 24: X-Rotor structural response simulated with an effective wind speed model with a mean wind speed of 12.5m/s

## 5 Conclusions

This control model presented in this report is a suitably computationally efficient model to allow for controller design, whilst including sufficient complexity to model the essential dynamic properties. As such, it can act as a transparent tool for prototyping controller designs, support controller analysis and design, and assess the effectiveness of controllers in meeting design objectives.

Detailed information on the design and implementation of the model has been given such that the internal operation of the model is clear and unambiguous. The model can support the X-Rotor project's immediate planned activities as described in the project plan. The next steps include,

- Comparison with higher fidelity simulations
- Facilitate the development of a set of linear models at linear operating points covering the full operational strategy to assist in controller design (Deliverable 3.3)
- Design of controllers for maximising power output below rated wind speed and controllers to limit power output to the rated power whilst minimising structural loads in above rated wind speeds (Milestone 9)
- Facilitate performance assessment of the X-Rotor concept (Deliverable 3.5)

## References

- Buhl Jr, M. L. (2005). A New Empirical Relationship between Thrust Coefficient and Induction Factor for the Turbulent Windmill State. *Technical Report NREL/TP-500-36834*.
- Campos-Gaona, D., Stock, A., Morgan, L., Leithead, W., & Anaya-Lara, O. (2021, 12). *X-rotor wp5 d5.1 secondary rotors and power train design (draft)*.
- Gaertner, E., Rinker, J., Sethuraman, L., Zahle, F., Anderson, B., Barter, G., ... Viselli, A. (2020). *Definition of the iea wind 15-megawatt offshore reference wind turbine technical report*. Retrieved from [www.nrel.gov/publications](http://www.nrel.gov/publications).
- Gala Santos, M. L. (2018). *Aerodynamics and wind-field models for wind turbine control* (Unpublished doctoral dissertation). University of Strathclyde.
- Jamieson, P. (2018). *Innovation in wind turbine design* (2nd ed.). Wiley.
- Leishman, J. (2016). *Principles of helicopter aerodynamics*. Cambridge University Press.
- Leithead, W. (2020, April). *Lecture notes in wind turbine loads*. University of Strathclyde - WAMESS CDT.
- Leithead, W., Camciuc, A., Amiri, A. K., & Carroll, J. (2019). The X-Rotor Offshore Wind Turbine Concept. *Journal of Physics: Conference Series*, 1356(1), 0–10. doi: 10.1088/1742-6596/1356/1/012031
- Marten, D., & Wendler, J. (2013). Qblade: an open source tool for design and simulation of horizontal and vertical axis wind turbines. *International Journal of Emerging Technology and Advanced Engineering*, 3, 264-269.
- Masson, C., Leclerc, C., & Paraschivoiu, I. (1998). Appropriate Dynamic-Stall Models for Performance. *International Journal of Rotating Machinery*, 4(2), 129–139.
- Moriarty, P., & Hansen, A. (2005). Aerodyn theory manual. *NREL*. doi: 10.1146/annurev.fl.15.010183.001255
- Murray, J., & Barone, M. (2011). The development of cactus, a wind and marine turbine performance simulation code. , 1-21. doi: 10.2514/6.2011-147
- Sharpe, D., & Freris, L. (1990). *Wind energy conversion systems*. Prentice Hall.

## Appendix A - Secondary rotor design

This appendix presents an overview of the methodology for specifying the secondary rotor design. As with the rest of this report, any numeric values are an illustrative choice of parameters only.

The X-Rotor system is kept in equilibrium through matching the primary rotor torque with the torque provided by the thrust acting on the secondary rotors. This is represented in equation 75, whereby the revolution averaged primary rotor torque  $\overline{M_\theta}$ , is matched by the revolution averaged thrust,  $\overline{T_s}$  of each of the  $N$  secondary rotors attached at the primary rotor radius  $R_p$ .

$$\underbrace{\left[ \frac{1}{\omega} \frac{1}{2} \rho A_P C_{PP} U_0^3 \right]}_{\overline{M_\theta}} = N R_P \underbrace{\frac{1}{2} \rho A_s C_{Ts} \omega_P^2 R_P^2 \left( 1 + \frac{1}{2} \lambda^{-2} \right)}_{\overline{T_s}}, \quad (75)$$

where  $C_{PP}$  represents the primary rotor power coefficient, and  $A_P$  represents the primary rotor area.

Utilising this relationship, the aerodynamic efficiency of power conversion between the primary and secondary rotors can then be readily obtained. This is achieved through representing the revolution averaged power from the secondary rotors as a fraction of the revolution averaged power captured by the primary rotor, giving

$$\eta_a = \frac{NP_s}{P_P} = \frac{NP_s}{\omega_P N R_P \overline{T_s}} = \frac{N \frac{1}{2} \rho A_s C_{Ps} \omega_P^3 R_P^3 \left( 1 + \frac{3}{2} \lambda^{-2} \right)}{\omega N R_P \frac{1}{2} \rho A_s C_{Ts} \omega_P^2 R_P^2 \left( 1 + \frac{1}{2} \lambda^{-2} \right)} = \frac{C_{Ps}}{C_{Ts}} \left( \frac{1 + \frac{3}{2} \lambda^{-2}}{1 + \frac{1}{2} \lambda^{-2}} \right). \quad (76)$$

The full rotor power coefficient is therefore given by

$$C_P = C_{PP} \eta = C_{PP} \frac{C_{Ps}}{C_{Ts}} \left( \frac{1 + \frac{3}{2} \lambda^{-2}}{1 + \frac{1}{2} \lambda^{-2}} \right). \quad (77)$$

This implies that the efficiency of power conversion between the primary and secondary rotors is driven by the ratio between the power and thrust coefficients which, in turn, can be maximised through lowering the axial induction factor of the secondary rotor.

Ideally, in below rated conditions the secondary rotors operate so as to perform traditional torque control on the primary rotor in order to facilitate maximum power point tracking. Equation 75 can once again be used, this time with the optimum values represented by a dash ('), to obtain the ideal operating point of the secondary rotors. This is given by

$$C'_{Ts} = \frac{A_P}{N A_s} \frac{C'_{PP}}{\left( \lambda'^3 + \frac{1}{2} \lambda' \right)}. \quad (78)$$

From this, it follows that in order to minimise the operational thrust coefficient - thus maximising the conversion efficiency, the secondary rotor area should be maximised.

The primary constraint on secondary rotor design is imposed by a maximum allowable tip-speed, imposed to avoid trans-sonic aerodynamic effects and limit acoustic emissions. This tip-speed limit is currently given by  $U_M = 184 \text{ m/s}$ , however further work is required to verify this initial estimate. This tip-speed limit is represented mathematically as

$$\omega_s R_s \leq U_M. \quad (79)$$

As the rotational speed typically has a lower limit imposed by the drive train configuration, the radius of the secondary rotor is constrained.

The tip-speed limit also manifests as a limit of the tip-speed ratio of the secondary rotors with

$$\lambda_s \leq \frac{U_M}{\lambda U_R}. \quad (80)$$

The secondary rotor therefore provides a unique and highly constrained design challenge. For a given primary rotor configuration, one must design a rotor to maximise the power to thrust coefficient ratio at the design thrust coefficient with a highly constrained tip-speed ratio.

In the case of the frequency constrained design, the rotational speed of the secondary rotor is limited by the minimum frequency of the drive-train at rated power,  $\omega_{g0}$ , and the fixed number of pole pairs in the generator.

$$\omega_s \geq \frac{\omega_{g0}}{p} \quad (81)$$

Combined with equation 79 this provides a limit on the rotor size with

$$R_s \leq \frac{pU_M}{\omega_{g0}}. \quad (82)$$

This radius is taken in its upper limit, so as to minimise the operational thrust coefficient and maximise the conversion efficiency. This also sets the tip-speed ratio as the upper limit presented in equation 80. Following this, the operational thrust coefficient can be calculated using equation 78.

With the operating point defined, the average axial induction,  $a_s$  can be calculated with

$$a_s = \frac{1}{2} \left( 1 - \sqrt{1 - \frac{C_{Ts}}{\int_0^1 F_h(x) dx}} \right), \quad (83)$$

where  $F_h(x)$  represents the tip-loss function, and  $x$  represents the non-dimensional radial coordinate. Whilst a number of tip-loss functions are available, this work uses the Prandtl function for horizontal axis rotors given by

$$F_h(x) = \frac{2}{\pi} a \cos \left( \exp \left[ -\frac{(1-x)N_s \lambda_s}{2(1-a_s)} \right] \right). \quad (84)$$

Here  $N_s$  represents the number of blades on the secondary rotor.

As this tip-loss function is dependent on the axial induction, a recursive scheme must be used to calculate the required axial induction. This can be achieved by initialising the tip-loss function as 1, calculating the induction using equation 83 then evaluating the tip-loss function with equation 84, and finally calculating the thrust coefficient with equation 85.

$$C_{Ts} = 4a_s(1-a_s) \int_0^1 F_h(x) dx. \quad (85)$$

This process can be repeated with the updated tip-loss function, until the realised thrust coefficient is equal to the thrust coefficient given by 85.

With the rotor radius, tip-speed ratio, and axial induction defined, the required rotor chord and twist distribution can be derived using analytical BEM methods. These relationships are provided by Jamieson (Jamieson, 2018) and they represent the BEM equations rearranged in their exact form. First the tangential induction can be evaluated using

$$a_{ts}(x) = \frac{\{\lambda_s^2 k^2 x^2 + 2\lambda_s kx - 4a_s k[\lambda_s x - k(1 - a_s)] + 1\}^{0.5} - (\lambda_s kx + 1)}{2\lambda_s kx}. \quad (86)$$

where  $k$  represents the glide ratio of the aerofoil. The tangential induction can then be utilised to find the non-dimensional lift distribution ( $\Lambda = cC_L/R_s$ ), which is required to achieve the desired induction. This is given by

$$\Lambda(x) = \frac{8\pi a(1 - a)}{N_s \lambda_s (1 + a_{ts}) \sqrt{(1 - a_s)^2 + \lambda_s^2 x^2 (1 + a_{ts})^2}} \frac{F_h}{\left[1 + \frac{(1 - a_s)}{k \lambda_s x (1 + a_{ts})}\right]}. \quad (87)$$

Through utilising a twist distribution given by

$$\beta(x) = \text{atan} \left[ \frac{(1 - a)}{\lambda_s x (1 + a_{ts})} \right] - \alpha_{design}, \quad (88)$$

where  $\alpha_{design}$  represents the design angle of attack for the aerofoil, it is ensured that the aerofoil will be operating at it's design angle of attack along the blade. This allows the design glide ratio  $k_{design}$  to be used in the calculation of tangential induction and non-dimensional lift distribution, and allows the blade chord to be recovered from the non-dimensional lift distribution with the design lift coefficient of the aerofoil section:

$$c(x) = \frac{\Lambda(x) R_s}{C_{Ldesign}}. \quad (89)$$

Prior to completing the preliminary rotor design, the aerofoil section(s) must be selected. Here, for simplicity, the rotor is designed using a single aerofoil section, the FFA\_W3\_241. This was chosen due to it's beneficial structural qualities, high aerodynamic performance, and the available aerodynamic data (Gaertner et al., 2020).

Utilising the above design methodology for a 5 bladed rotor, the chord and twist distributions for the secondary rotor are shown in Figure 25.

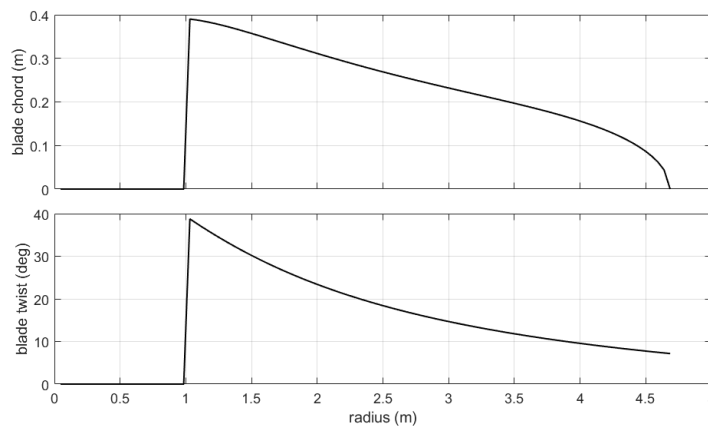
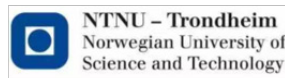


Figure 25: Secondary rotor chord and twist distribution

## Consortium



## Disclaimer

All information provided reflects the status of the XROTOR project at the time of writing and may be subject to change.

Neither the XROTOR Consortium as a whole, nor any single party within the XROTOR Consortium warrant that the information contained in this document is capable of use, nor that the use of such information is free from risk. Neither the XROTOR Consortium as a whole, nor any single party within the XROTOR Consortium accepts any liability for loss or damage suffered by any person using the information.

This document does not represent the opinion of the European Community, and the European Community is not responsible for any use that might be made of its content.

## Copyright Notice

© 2022 by the authors, the XROTOR Consortium. This work is licensed under a ["CC BY 4.0"](https://creativecommons.org/licenses/by/4.0/) license.

